

Low Surface Brightness structures from annotated deep CFHT images: effects of the host galaxy’s properties and environment

Elisabeth Sola,^{1,2} Pierre-Alain Duc,² Mathias Urbano,² Felix Richards,³ Adeline Paiement,⁴ Michal Bílek,^{5,6,7} Mustafa K. Yıldız,^{8,9} Alessandro Boselli,¹⁰ Patrick Côté,¹¹ Jean-Charles Cuillandre,¹² Laura Ferrarese,¹¹ Stephen Gwyn,¹¹ Olivier Marchal,² Alan W. McConnachie,¹¹ Matthieu Baumann,² Thomas Boch,² Florence Durret,¹³ Matteo Fossati,^{14,15} Rebecca Habas,¹⁶ Francine Marleau,¹⁷ Oliver Müller,¹⁸ Mélina Poulain,¹⁹ Vasily Belokurov¹

¹ *Institute of Astronomy, Madingley Rd, Cambridge CB3 0HA, UK*

² *Université de Strasbourg, CNRS, Observatoire astronomique de Strasbourg (ObAS), UMR 7550, F-67000 Strasbourg, France*

³ *Department of Computer Science, Swansea University, UK*

⁴ *Université de Toulon, Aix Marseille Univ, CNRS, LIS, Marseille, France*

⁵ *Collège de France, 11 place Marcelin Berthelot, 75005 Paris, France*

⁶ *LERMA, Observatoire de Paris, CNRS, PSL Univ., Sorbonne Univ., 75014 Paris, France*

⁷ *Department of Astrophysics, University of Vienna, Türkenschanzstraße 17, 1180 Vienna, Austria*

⁸ *Astronomy and Space Sciences Department, Science Faculty, Erciyes University, Kayseri, 38039, Türkiye*

⁹ *Erciyes University, Astronomy and Space Sciences Observatory Applied and Research Center (UZAYBİMER), 38039, Kayseri, Türkiye*

¹⁰ *Aix-Marseille Univ., CNRS, CNES, LAM, Marseille, France*

¹¹ *Herzberg Astronomy and Astrophysics Research Centre, National Research Council of Canada, Victoria, BC V9E 2E7, Canada*

¹² *Université Paris-Saclay, Université Paris Cité, CEA, CNRS, AIM, 91191, Gif-sur-Yvette, France*

¹³ *Sorbonne Université, CNRS, UMR 7095, Institut d’Astrophysique de Paris, 98bis Bd Arago, 75014 Paris, France*

¹⁴ *Dipartimento di Fisica G. Occhialini, Università degli Studi di Milano-Bicocca, Piazza della Scienza 3, 20126 Milano, Italy*

¹⁵ *INAF - Osservatorio Astronomico di Brera, via Brera 28, 21021 Milano, Italy*

¹⁶ *INAF-Astronomical Observatory of Abruzzo, Via Maggini, 64100, Teramo, Italy*

¹⁷ *Universität Innsbruck, Institut für Astro- und Teilchenphysik, Technikerstr. 25/8, 6020 Innsbruck, Austria*

¹⁸ *Institute of Physics, Laboratory of Astrophysics, Ecole Polytechnique Fédérale de Lausanne (EPFL), 1290 Sauverny, Switzerland*

¹⁹ *Space Physics and Astronomy Research Unit, University of Oulu, P.O. Box 3000, FI-90014, Oulu, Finland*

Accepted XXX. Received YYY; in original form ZZZ

ABSTRACT

Hierarchical galactic evolution models predict that mergers drive galaxy growth, producing low surface brightness (LSB) tidal features that trace galaxies’ late assembly. These faint structures encode information about past mergers and are sensitive to the properties and environment of the host galaxy. We investigated the relationships between LSB features and their hosts in a sample of 475 nearby massive galaxies spanning diverse environments (field, groups, Virgo cluster) using deep optical imaging from the Canada-France-Hawaii Telescope (MATLAS, UNIONS/CFIS, VESTIGE, NGVS). Using Jafar, an online annotation tool, we manually annotated tidal features and extended stellar haloes, including 199 tidal tails and 100 streams. Geometric and photometric measurements were extracted to analyse their dependence on galaxy mass, environment, and internal kinematics. At our surface brightness limit of 29 mag arcsec⁻², tidal features and stellar haloes contribute 2% and 10% of total galaxy luminosity, respectively. Tidal features are detected in 36% of galaxies, with none fainter than 27.8 mag arcsec⁻². The most massive galaxies are twice as likely to host tidal debris, and for early-type galaxies their haloes are twice as luminous as those in lower-mass systems, a trend not observed in late-type galaxies. Although small-scale interactions increase the frequency of tidal features, the large-scale environment does not influence it. An anticorrelation between this frequency and rotational support is found, but may reflect the mass-driven effect. We release our database of annotated features for deep learning applications. Our findings confirm that galaxy mass is the dominant factor influencing tidal feature prevalence, consistent with hierarchical formation models.

Key words: Galaxies: interactions – Galaxies: evolution – Methods: data analysis

1 INTRODUCTION

In the framework of hierarchical models of galaxy evolution, galaxies are expected to be assembled through mergers and smooth accretion

of cold intergalactic gas. The dominant growth mode is a function of time, environment, mass and morphological type (e.g., [White & Frenk 1991](#); [Kauffmann et al. 1993](#); [Cole et al. 2000](#); [Baugh et al. 2003](#); [Kereš et al. 2005](#); [Daddi et al. 2007](#); [Ocvirk et al. 2008](#); [Dekel et al. 2009](#); [Förster Schreiber et al. 2009](#); [Agertz et al. 2009](#); [Stringer & Benson 2007](#); [Genel et al. 2010](#); [L’Huillier et al. 2012](#)). Massive early-type galaxies (ETGs) are most likely formed in a two-phase scenario first dominated by smooth accretion of gas and gas-rich mergers and then by minor mergers (e.g. [Oser et al. 2010](#); [Thomas et al. 1999](#); [Naab et al. 2009](#)) or more rarely from the merger of two spirals (e.g., [Toomre 1977](#); [Barnes 1988](#)). In contrast, the formation of late-type galaxies (LTGs) is likely smoother, mainly through accretion of cold intergalactic gas (e.g., [Sancisi et al. 2008](#); [Bílek et al. 2023](#)). The environment in which galaxies reside also drives their evolution, which has been confirmed observationally and with numerical simulations (e.g., [Gunn & Gott 1972](#); [Oemler 1974](#); [Dressler 1980](#); [Larson et al. 1980](#); [Byrd & Valtonen 1990](#); [Moore et al. 1996](#); [Bekki 1999](#); [Goto et al. 2003](#); [Mihos 2003](#); [Hester 2006](#); [Kawata & Mulchaey 2008](#); [Berrier et al. 2008](#); [Boselli et al. 2022](#)).

Mergers and interactions between galaxies lead to various modifications of galaxies’ properties, such as their morphology, kinematics, chemical composition, stellar metallicity and age gradients (e.g., [Balcells & Quinn 1990](#); [Di Matteo et al. 2009](#); [Bois et al. 2011](#); [Schulze et al. 2017](#); [Amorisco 2016](#); [Bílek et al. 2023](#)). Such interactions produce tidal structures that extend around galaxies. The nature, morphology, and lifetime of these features highly depend on the age, mass, type, and impact parameters of the collisions and mergers. The mass ratio between the interacting galaxies, the inclinations of their orbits and differences in velocities are essential parameters (e.g., [Pop et al. 2018](#); [Mancillas et al. 2019](#); [Karademir et al. 2019](#)). For instance, tidal tails are likely formed during major mergers (e.g., [Arp 1966](#); [Toomre & Toomre 1972](#)), streams are presumably formed during minor mergers (e.g., [Bullock & Johnston 2005](#); [Belokurov et al. 2006](#)), and shells are typically formed during intermediate-mass radial mergers (e.g., [Quinn 1984](#); [Priour 1990](#)). Hence, the different types of tidal structures hold crucial clues about the assembly history of galaxies. Numerical simulations in cosmological contexts help to interpret the prevalence and frequency of tidal features and extended stellar haloes (e.g., [Hernquist & Quinn 1987](#); [Johnston et al. 1999](#); [Ibata et al. 2001b](#); [Johnston et al. 2008](#); [Cooper et al. 2010](#); [Lux et al. 2013](#); [Ebrova 2013](#); [Hendel & Johnston 2015](#); [Thomas et al. 2017](#); [Pop et al. 2018](#); [Hood et al. 2018](#); [Mancillas et al. 2019](#); [Bílek et al. 2023](#)).

Tidal features are also affected by the environment in which they reside. In the field, without external perturbations, stripped tidal debris remains loosely bound and can be visible for several Gyr (e.g., [Mancillas et al. 2019](#)). In clusters, they are the result of competing processes that can either generate or erase them (e.g., [Byrd & Valtonen 1990](#); [Moore et al. 1996](#); [Mihos 2003](#); [Gnedin 2003](#)). The diffuse debris contributes to the intracluster light (ICL), which is made of stars no longer bound to any galaxy (e.g., [Rudick et al. 2006](#); [Conroy et al. 2007](#); [Rudick et al. 2009](#); [Montes 2019](#)).

While a wealth of tidal features have been observed in the Local Group (e.g., [Ibata et al. 2001a](#); [Belokurov et al. 2006](#); [McConnachie et al. 2009](#); [Martin et al. 2014](#)), their detection is challenging for objects located further away that are no longer resolved into stars. The diffuse, Low Surface Brightness (LSB), light they emit is difficult to detect. Unveiling the faint diffuse tidal features requires LSB optimized deep imaging as well as dedicated reduction pipelines. Recent progress in CCD cameras, observing strategies and data processing techniques enabled us to reach the LSB regime (> 25 mag arcsec $^{-2}$) with appropriate background subtraction (e.g., [Magnier & Cuillan-](#)

[dre 2004](#); [Borlaff et al. 2019](#)). Deep observations of several hundreds of square degrees have been conducted using a large number of telescopes, from small-aperture telescopes (e.g., [Martínez-Delgado et al. 2010](#); [Abraham & van Dokkum 2014](#); [Spitler et al. 2019](#); [Mosenson et al. 2020](#)) to large ones (e.g., [Mihos et al. 2005](#); [Ferrarese et al. 2012](#); [Boselli et al. 2018](#); [Duc 2020](#); [Venhola et al. 2017](#); [Iodice et al. 2021](#); [Alabi et al. 2020](#); [Jackson et al. 2021](#)). The upcoming Euclid and Rubin/LSST surveys are about to extend the realm of the LSB Universe even further, with thousands of square degrees covered (e.g., [Euclid Collaboration et al. 2022](#); [Martin et al. 2022](#)).

Different methods have been developed to identify tidal features in deep images. Among them, the basic visual inspection of images conducted by one or more collaborators remains popular (e.g., [Tal et al. 2009](#); [Atkinson et al. 2013](#); [Morales et al. 2018](#); [Hood et al. 2018](#); [Müller et al. 2019](#); [Kluge et al. 2020](#); [Bílek et al. 2020](#); [Jackson et al. 2021](#)). For samples of thousands of galaxies, simple classification tasks can also be done by a crowd of citizen scientists (e.g., [Casteels et al. 2013](#)). However, as the sample size increases, visual detection is no longer possible, and it is necessary to rely on automated techniques (e.g., [Pawlik et al. 2016](#); [Mantha et al. 2019](#); [Kado-Fong et al. 2018](#)). Non-parametric methods like the Gini- M_{20} parameter (e.g., [Abraham et al. 2003](#); [Lotz et al. 2004](#)) or the CAS system (e.g., [Conselice et al. 2003](#); [Conselice 2009](#)) are also used to characterise the host galaxies. However, they are weakly sensitive to the presence of the LSB structures of interest. Deep learning and convolutional neural networks (CNNs) provide promising approaches (e.g., [Pearson et al. 2019](#); [Walmsley et al. 2019](#); [Martin et al. 2020](#); [Bickley et al. 2021](#)) but remain to be thoroughly tested on complex images.

Several limitations arise from the aforementioned studies. First, automated methods still need to provide subtle classifications and distinctions between the different types of tidal features. Furthermore, quantitative measurements of the properties of LSB tidal features that are obtained consistently over large samples of galaxies are still missing. However, they are needed to constrain specific models of galactic evolution. So far, most studies focused on the census of tidal debris have performed qualitative analyses (e.g., [Tal et al. 2009](#); [Miskolczi et al. 2011](#); [Casteels et al. 2013](#); [Morales et al. 2018](#); [Bílek et al. 2020](#)). Those that have provided quantitative results relied on limited samples (e.g., [Martínez-Delgado et al. 2021](#); [Huang & Fan 2022](#)).

[Sola et al. \(2022\)](#) introduced a dedicated annotation tool, *Jafar*, and an associated database, which partially address these difficulties. They enable the retrieval of quantitative measurements of LSB tidal features through the precise delineation of features superimposed on deep images. This online tool¹ allows contributors to annotate images of hundreds of galaxies in a user-friendly way.

This paper is a follow-up of a series of studies based on the census of LSB structures ([Duc et al. 2015](#); [Bílek et al. 2020, 2023](#); [Sola et al. 2022](#)) identified in the ATLAS^{3D} ([Cappellari et al. 2011a](#)) volume-limited sample of massive nearby galaxies. In particular, [Bílek et al. \(2020, 2023\)](#) performed a comprehensive study of tidal features around ETGs. They investigated the origin of the differences in rotational support among ETGs in the field and groups. They found that the kinematics of the ETGs were established early in the formation history of the galaxies. Complementary to that study, and others carried out at higher redshifts (e.g., [Bridge et al. 2010](#); [Wen & Zheng 2016](#)), we investigate the late galactic evolution in this paper. We probe the merger history within the past few Gyr for which the

¹ *Jafar* relies on developments made by a computer vision team ([Richards et al. 2022, 2023](#)) and the CDS Aladin team.

LSB features visible today may bring observational constraints. We extend the previous sample of Břlek et al. (2020) by including LTGs and the Virgo cluster as an additional environment. We target galaxies undergoing interactions and post-merger systems without knowing whether they host tidal features.

The article is organised as follows. In Section 2, we present the data and galaxy sample, and our methods are explained in Section 3. We present the general properties of LSB features in Section 4. Results concerning the effect of galaxy mass and environment on tidal features and haloes are presented in Sections 5 and 6, respectively, while their joint impact is shown in Section 7 and the impact of internal kinematics is presented in Section 8. We discuss the results and compare them to the literature in Section 9, and the conclusions are presented in Section 10.

2 SAMPLE AND DATA

This section describes the data we used to probe galactic growth through LSB tidal features. Briefly, we analyse galaxies extracted from the reference sample compiled by the ATLAS^{3D} collaboration (Cappellari et al. 2011a), that contains 260 ETGs (the primary target of the ATLAS^{3D} project) and 611 LTGs (from their parent sample). Our final galaxy sample is composed of the galaxies from the ATLAS^{3D} reference sample that lie in the footprint of our images. We detail the characteristic of the galaxies catalogues and images below.

ETGs and LTGs from the ATLAS^{3D} reference sample are characterised by being bright (absolute magnitude in K -band $M_K < -21.5$ mag), massive (stellar mass $M_\star > 6 \times 10^9 M_\odot$), nearby (distance $D < 42$ Mpc), and visible from the Northern hemisphere ($|\delta - 29^\circ| < 35^\circ$ and $|b| > 15^\circ$ with δ the declination and b the galactic latitude). This reference sample probes different environments, i.e., field, groups, and the Virgo cluster located at 16.5 Mpc (Gavazzi et al. 1999; Mei et al. 2007; Cantiello et al. 2018). The distinction between ETGs and LTGs is based on the morphology of galaxies, i.e. the presence of spiral arms or prominent spiral arms (Cappellari et al. 2011a). As the focus of the ATLAS^{3D} project, ETGs also have integral field unit (IFU) kinematic information available. This enables one to separate ETGs between fast rotators, that have regular rotation patterns, and slow rotators. Such a distinction is relevant as it is linked to the formation pathways of ETGs. Such kinematic information is missing for the LTG sample, but it is expected that LTGs are all fast rotators as suggested by their spiral pattern.

We used deep images from the 3.6-meter Canada-France-Hawaii Telescope (CFHT) obtained with the wide-field optical imager MegaCam. MegaCam offers a pixel size of 0.187 arcsecond per pixel and a field of view of $1^\circ \times 1^\circ$. We utilised images originating from four surveys carried out at the CFHT: the Mass Assembly of early-Type GaLaxies with their fine Structures survey (MATLAS², Duc et al. 2015); the Canada-France Imaging Survey (CFIS³, Ibata et al. 2017); the Virgo Environmental Survey Tracing Ionised Gas Emission (VESTIGE⁴, Boselli et al. 2018); and the Next Generation Virgo Cluster (NGVS⁵, Ferrarese et al. 2012).

The main goals, observing strategies and available photometric bands of these four deep CFHT surveys differ. NGVS imaged the 104 square degrees of the Virgo cluster in four bands (u , g , i , z and a few

pointings in the r -band). VESTIGE, a blind narrow-band $H\alpha$ + $[\text{NII}]$ imaging survey, covered the same footprint as NGVS. VESTIGE also acquired r -band images of the whole cluster for calibration purposes and to subtract the continuum emission.

MATLAS targeted nearby massive ETGs from the ATLAS^{3D} sample through pointed observations in g and r -bands (as well as in u and i for some galaxies). CFIS is a blind survey targeting 5,000 square degrees in the Northern Hemisphere in u and r -bands, with additional bands available from observations made with other telescopes as part of the Ultraviolet Near Infrared Optical Northern Survey (UNIONS) project⁶. All the NGVS bands, MATLAS bands, VESTIGE r -band and CFIS r -band images were processed through the LSB-optimised reduction pipeline Elixir-LSB (Cuillandre, private communication, Duc et al. 2015) to enhance any faint structures. As a result of this processing, surface brightness limits of 29 mag arcsec⁻² in the g -band for NGVS (Ferrarese et al. 2012), 28.9 mag arcsec⁻² for MATLAS r -band, 28.3 mag arcsec⁻² for CFIS r -band (Cuillandre, private communication), and 27.2 mag arcsec⁻² for VESTIGE r -band⁷ (Boselli et al. 2018) are reached. Note that these values depend on the definition used, and can vary from one image to the other⁸.

The important aspect is that the same reduction pipeline was applied on images from the same telescope, instrument, and band⁹, which made the deep images look relatively similar. The work in this study is based on the LSB r -band images from CFIS, MATLAS and VESTIGE, which was supplemented with g -band data for colour information, when available from NGVS and MATLAS. The r -band was chosen as the reference band as it is the only CFIS band on which the Elixir-LSB pipeline has been run; and because MATLAS and VESTIGE also had available Elixir-LSB-processed r -band images. Table 1 summarises the properties of these CFHT surveys.

We used Multi-Order Coverage maps (MOCs, Fernique et al. 2014) to determine which galaxies from the ATLAS^{3D} reference sample had available CFHT LSB-optimised r -band images. We obtained a final sample of 475 galaxies, among which are 244 ETGs and 231 LTGs. Table 2 details the number of galaxies as a function of the survey and environment. The complete list of our galaxies and their basic properties are presented in Table A1. Some galaxies present in CFIS images had already been observed by MATLAS. In that case, we preferentially used the MATLAS images.

For data processing, we followed the procedures detailed in Sola et al. (2022). We cropped the images around the galaxies of interest, keeping a field of view of $31' \times 31'$, large enough to cover the extended LSB structures around them. Images were then binned by a factor of three, and a modified inverse hyperbolic sine scaling,

⁶ The UNIONS project is a collaboration of wide field imaging surveys of the northern hemisphere. UNIONS consists of the Canada-France Imaging Survey (CFIS), conducted at the 3.6-meter CFHT on Maunakea, members of the Pan-STARRS team, and the Wide Imaging with Subaru HyperSuprime-Cam of the Euclid Sky (WISHES) team. CFHT/CFIS is obtaining u and deep r bands; Pan-STARRS is obtaining deep i and moderate-deep z band imaging, and Subaru/WISHES is obtaining deep z band imaging.

⁷ Boselli et al. (2018) reach 25.8 mag arcsec⁻² at 1σ for a scale of 2.8 arcsec which can be converted to about 27.2 mag arcsec⁻² at 1σ for a scale of 10 arcsec.

⁸ In Appendix E we consistently re-compute the surface brightness limits for our surveys using a single method. CFIS and MATLAS have slightly higher depths than quoted by the literature, while VESTIGE is deeper than quoted. As noted, the surface brightness limit may not be the best parameter to assess the detectability of the LSB structures studied here.

⁹ In Appendix F we discuss the impact of the filter change on MegaCam between CFIS/VESTIGE and MATLAS/NGVS

² MATLAS, <http://obas-matlas.u-strasbg.fr>

³ CFIS, <https://www.cfht.hawaii.edu/Science/CFIS/>

⁴ VESTIGE, <https://mission.lam.fr/vestige/index.html>

⁵ NGVS, <http://astrowww.phys.uvic.ca/lff/NGVS/Home>

Table 1. Properties of the CFHT surveys utilised in this work.

Survey	Band used ^a	Exposure time [s]	Targets	Footprint area [deg ²]
NGVS ^b	<i>Old g</i>	5 × 634	Virgo cluster	116
VESTIGE	<i>New r</i>	12 × 60	Virgo cluster	116
MATLAS	<i>Old r (+ old g)</i>	7 × 345	Group ETGs	310
CFIS	<i>New r</i>	Varying ^c	Blind survey	5,000

^a MegaCam’s filter set has been changed in 2015; the filters used before 2015 are denoted as *Old* and the ones in use afterwards are denoted as *New*. See Appendix F for more details.

^b NGVS *g*-band images were only used for colour information, not for the detection and analysis of tidal features.

^c The integration time is adjusted based on instant observing conditions (atmosphere, image quality, sky background) to ensure that the full depth within the 3 exposures will be uniform across the whole survey footprint, <https://www.cfht.hawaii.edu/Science/CFIS/cfissurvey.html>.

asinh, was applied to enhance the faintest structures. The surface brightness (SB) maps in units of mag arcsec⁻² were computed using Equation 2 of Sola et al. (2022). Finally, the images were converted to the HiPS format (see Fernique et al. 2015) and uploaded to the *Jafar* annotation tool. In addition to our deep images, we used the shallower composite colour images of the DR1 PanSTARRS¹⁰ imaging survey (Chambers et al. 2016), available at CDS, to characterise the brightest inner regions of the galaxies. PanSTARRS covers the entire sky north of -30° in declination in five bands (*g*, *r*, *i*, *z* and *y*). In Figures A1 and A2, we present color-composite images of our galaxies, with the greyscale corresponding to the deep image and the colour image to a combination of PanSTARRS *r*, *g*, *i* images.

Our final sample of 475 galaxies is composed of 94% of the 260 ETGs and 38% of the 611 LTGs from the ATLAS^{3D} reference sample. They are located in different environments, from the field to a cluster. Note that we only have one cluster environment, Virgo, which is still dynamically young and not representative of all the cluster types (e.g., Binggeli et al. 1987; Boselli et al. 2014). The environment is parameterised by the environment density, ρ_{10} defined as the mean density of galaxies in a sphere centred on the target galaxy and containing the ten closest neighbours (Cappellari et al. 2011b). Galaxies in the Virgo cluster typically have $\log_{10}(\rho_{10}) > -0.4$. Our sample includes 88% of Virgo galaxies in the reference sample (98% of all Virgo ETGs and 79% of all Virgo LTGs). Outside the cluster, our sample contains 49% of the reference sample (93% of all field ETGs and 33% of all field LTGs).

In Figure 1, we present the main properties of our 475 galaxies. The left panel shows the absolute *K*-band magnitude, M_K , as a function of the distance, *D*, while the right panel displays the stellar mass as a function of the environment density, ρ_{10} . The overdensity of galaxies around 16.5 Mpc is due to the Virgo cluster. We do not have in our sample some of the closest and furthest LTGs from the ATLAS^{3D} reference sample; as those reference LTGs are located at a median distance of 29 Mpc against 25.4 Mpc for our selected LTGs. As seen in the right plot, our selected ETGs are more massive (median mass of $3.3 \times 10^{10} M_\odot$) than our selected LTGs (median mass of $2.2 \times 10^{10} M_\odot$), which is also the case for the reference sample. The marginal histogram over environment density shows two trends. First, our selected ETGs and LTGs are located in similar environments, which makes further comparisons simpler. Second, compared

to the reference LTGs, we miss some LTGs in regions of low- and intermediate-densities (i.e., in the densest regions of galaxy groups, below the Virgo cluster density). We are indeed biased towards LTGs located in the ETG-rich groups observed by MATLAS¹¹, which is not fully compensated by the availability of the blind CFIS images.

3 METHODS

In this section, we present *Jafar*, the annotation tool used to study the LSB tidal features in our deep images. We describe how we characterised these structures, in terms of shape and luminosity.

3.1 The *Jafar* annotation server

Sola et al. (2022) introduced a web-based annotation tool that enables contributors, preferentially trained experts, to delineate precisely the shapes of LSB structures superimposed on deep images. Here we name it *Jafar*¹², standing for Just Annotate Features for Astronomical Results¹³. This user-friendly interactive tool provides efficient ways to visualise and navigate through images, draw features and label the annotations.

Each galaxy can be annotated by several contributors¹⁴. Contributors are asked to delineate the contours of LSB features by choosing the most appropriate drawing shape among several (e.g. ellipses, polygons, circles, rectangles, or cubic Bézier curved lines) and attach a corresponding label. All drawn shapes are summarised in a table and can later be modified. Once the annotation is done, the coordinates in right ascension and declination of the contours of the shapes are stored in a database, along with the corresponding label. As contributors are asked to annotate every relevant feature, several drawn shapes are superimposed on each image.

Features of interest can be labeled as *Inner galaxy*, *Halo*, *Tidal Tails*, *Streams*, *Shells*, *Companion Galaxy*, *Cirrus*, *Ghost Reflections*, *Satellite Trails*, *Instrument* or *High Background*. They can be categorized as one of two broad types: stellar light and contamination

¹¹ MATLAS pointings targeted group ETGs, but in some images group LTGs were also observed.

¹² *Jafar*, <https://jafar.astro.unistra.fr/>

¹³ And a nod to the names of the services provided by CDS, Aladin, Simbad or Vizier.

¹⁴ Contributors can see only their own annotations.

¹⁰ PanSTARRS, <https://panstarrs.stsci.edu/>

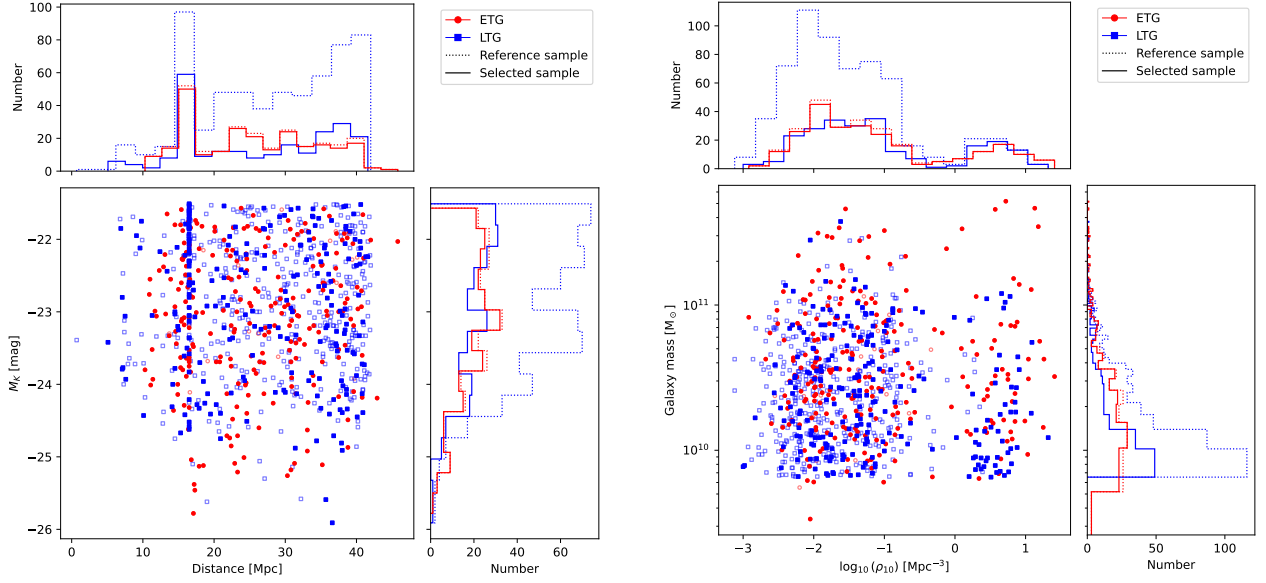


Figure 1. Main properties of our final sample of 475 galaxies, compared to the reference sample from the ATLAS^{3D} project. ETGs are plotted in red and LTGs in blue. The solid lines and filled circles correspond to our final sample, while the dotted lines and open circles correspond to the reference sample. *Left:* Scatter plot of the absolute K -band magnitude M_K (in mag) versus the distance (in Mpc) of galaxies from our final sample, the ATLAS^{3D} reference sample, and their marginal histograms. *Right:* Scatter plot of the galaxy stellar mass (in M_\odot) as a function of the environment density ρ_{10} (in Mpc^{-3}) of galaxies from our final sample, the ATLAS^{3D} reference sample, and their marginal histograms. Galaxies in the Virgo cluster typically have $\log_{10}(\rho_{10}) > -0.4$.

Table 2. Number of galaxies studied in this work, according to the survey used to image them, their morphological type and Virgo membership.

Type	Virgo ETGs	Virgo LTGs	Field ETGs	Field LTGs	Total
MATLAS	5	4	174	49	232
CFIS	0	0	7	113	120
VESTIGE	52	51	6	14	123
Total	57	55	187	176	475

sources, the light of which hinders the annotation process. Starting with stellar components, the *Inner galaxy* is defined as the central region of the target galaxy, encompassing the most luminous features. Contributors were invited to display the shallow PanSTARRs images to draw this specific bright component. For LTGs, the *Inner galaxy* annotation delineates the region with the prominent spiral arms and bars. For ETGs the drawn ellipse encloses all the light visible in the displayed shallow image, corresponding de facto to an isophotal limit. In Figures A1 and A2, the area covered by the *Inner galaxy* annotation corresponds to the region in true colour. The *Halo* annotation is the extended LSB stellar halo, generally elliptical, only visible in deep images (i.e., the greyscale part in Figures A1 and A2). It extends from the external boundaries of the inner galaxy up to the external boundary of the galaxy visible in deep images, and has thus a ‘donut’ shape. One should remember that the respective regions covered by the *Inner galaxy* and *Halo* annotations are subjective, and the latter should be used with caution. However they provide a quick direct way to disclose trends that can later be quantified with proper aperture photometry. Besides, even if our measurements strongly depend on our working definition of the halo (in a context whether there is no consensus on it), it allows us to investigate trends within our large sample in a consistent way. They are also of special utility for training automated ML-based algorithms. In addition, it is important to note that for LTGs, we cannot distinguish between a proper halo

with a 3D structure and a thick stellar disc with no spiral arms. Geometric effects (orientation) are not taken into account. It must also be noted that the more conventional definition of a halo, i.e. the stellar outskirts of galaxies composed of a mixture of in-situ and accreted stars (e.g., McCarthy et al. 2012; Cooper et al. 2013; Rich et al. 2019), is best seen for nearly edge-on LTGs (e.g., Mosenkov et al. 2020), but it cannot be properly disentangled from photometry alone for ellipticals and face-on disks. This implies that the measurements of our haloes for LTGs are probably upper limits compared to the more conventional definition.

For delineating tidal features, we follow the definitions established in the previous papers of this series (e.g., Duc et al. 2015; Bílek et al. 2020; Sola et al. 2022). We refer to Figures 3 and 4 of Sola et al. (2022) for illustrations of each type of structure defined here. We consider *Tidal Tails* as elongated material that appears to originate from the target galaxy and presumably formed during major mergers (e.g., Arp 1966; Toomre & Toomre 1972; Mihos 1995). On the contrary, *Streams* likely originate from minor mergers (e.g., Bullock & Johnston 2005; Belokurov et al. 2006; Martínez-Delgado et al. 2010). The low-mass companions from which *Streams* emanate may be visible on the image or not. Therefore orphan structures with no obvious progenitors are considered as streams. Although tails and streams are generated by the same process, i.e. tidal interaction with another companion galaxy, the distinction we make is based on the

point of view of the target, the massive galaxy in the field. This enables us to obtain a more subtle disentanglement of the types of involved mergers (major or minor).

Shells are arc-shaped, often concentric, features that tend to form during intermediate-mass radial mergers (e.g., [Prieur 1990](#); [Ebrowa 2013](#); [Duc et al. 2015](#); [Pop et al. 2018](#)). Nearby *Companion* galaxies with a mass similar to the target galaxy and a slight velocity difference (about 200 km s^{-1})¹⁵ are also delineated.

Contributors also annotated several contaminants, including *Cirrus*, the dust clouds from our own Galaxy that scatter the optical light, and circular *Ghost reflections*, i.e. artificial haloes around bright sources, such as foreground stars or galaxies that result from internal light reflections in the instrument. Moreover *Satellite Trails*, *Instrument* artefacts such as CCD gaps and regions having *High Background* values of unknown origin may also be drawn with the annotation tool. We used the *High Background* label in this study when the LSB structures of interest were contaminated.

[Sola et al. \(2022\)](#) addressed the issue of determining which annotation to keep when a given structure was annotated by several contributors to avoid duplicates. To that end, we applied in this paper the selection process described in Section 4.8 of [Sola et al. \(2022\)](#), and we briefly summarise it in Section 4.1. We only used annotations conserved after that selection process (unless explicitly mentioned otherwise).

All our 475 galaxies have been annotated by at least two contributors out of four. One contributor annotated 100% of the galaxies, while three others annotated 74%, 69% and 22% of our sample. Table 3 summarises the number of annotations stored in the database as a function of their type. The middle column indicates the total number of annotations by all contributors, including the duplicates, while the right column indicates the number of annotations kept after the selection process. We eliminated duplicates, merging common annotations. We only kept tidal tails whose progenitor is the target galaxy in order to avoid counting tails originating from a companion galaxy twice. Twenty haloes were impossible to annotate due to contamination sources (bright foreground star or high background) overlapping with the galaxy. These 455 haloes, 199 tidal tails and 100 streams are used to derive the results presented in this paper.

We publicly release Tables B1 and Table B2, which list all the individual tails and streams along with some of their properties such as geometry, SB and luminosity, as well as the number of tidal features per galaxy and halo properties. In Appendix B, we provide a file containing the coordinates of the contours of the individual features (presented as polygons) in a format readable by Aladin and SAOImageDS9.

3.2 Computing the shapes and luminosity of LSB features

The database of drawn annotations provides quantitative information about LSB structures. Geometrical analyses are presented in [Sola et al. \(2022\)](#). To summarise, we computed geometrical properties such as the area, length, width and radii of shells from the contours of the annotations. We also created masks of the annotations that we applied on the surface brightness maps to automatically retrieve characteristic SB values of the annotated features. A similar process yielded $g - r$ colour values.

In this work, we refine our SB measurements by performing background subtraction to remove the excess light coming from bright

Table 3. Number of annotations stored in the database as a function of their type. *Total* refers to the total number of annotations made by all users, while *Selected* reflects the number of annotations kept after the selection process, that affects *Inner Galaxy*, *Halo*, *Tidal Tails* and *Streams*, and used in our analysis.

Annotation type	Total	Selected
Inner Galaxy	1259	475
Halo	1193	455
Tidal Tails	616	199
Streams	202	100
Shells	311	311
Companion Galaxy	991	991
High Background	1307	1307
Ghosted Halo	5343	5343
Cirrus	317	317
Satellite Trail	114	114
Instrument	467	467
Total	11832	10081

sources or from overlapping annotations. Previously, we used the median value as the most representative SB value in each annotation, which enabled us to obtain results very quickly from our masks. Here, we developed a method to obtain more precise measurements of the luminosity and SB inside annotated features at the cost of longer computation times. The process is described in Appendix C. Briefly, even though the background is supposed to be constant after being processed by Elixir-LSB, local variations still exist due to contamination sources and must be removed. To that end, we remove bright sources from the masks of the annotations, we then estimate a new background value that we later subtract from the masks. These background-corrected values of luminosity and SB are presented in this paper.

3.3 Statistical tests

In the following sections, tests are applied to determine whether trends are statistically significant. The t-test¹⁶ ([Student 1908](#)) tests the null hypothesis that two independent samples have the same mean, while the 2-sample Kolmogorov-Smirnov (KS)¹⁷ ([Hodges 1958](#)) tests the null hypothesis that two samples come from the same distribution. Mood's test¹⁸ ([Mood 1950](#)) is used to test the null hypothesis that two samples come from populations with the same median. The Z-test, testing can be applied to check whether the proportions from two populations are the same. Pearson's r ¹⁹ ([Pearson 1895](#)) and Spearman's r ²⁰ ([Spearman 1904](#)) are applied to test linear correlations and monotonic relationships, respectively. If the conditions of applications of the tests are verified, and if the p-value of the tests is lower than a given threshold, namely 0.05 for a confidence level of 5% (or two-sigma), the null hypothesis can be rejected. We chose for the analyses below a threshold of 5% to reject the null hypothesis and to consider the result of a test to be statistically significant.

¹⁶ [Scipy's stats.ttest_ind](#)

¹⁷ [Scipy's 2-sample KS test](#)

¹⁸ [Scipy's Mood's median test](#)

¹⁹ [Scipy's Pearson's r test](#)

²⁰ [Scipy's Spearman's r test](#)

¹⁵ This threshold was chosen to ensure that the two galaxies currently involved in a tidal interaction are able to produce visible tidal debris.

Table 4. Mean number of tidal features per galaxy, taking into account all the galaxies, even those without tidal features. In parenthesis is indicated the mean number of features per galaxy computed only for the galaxies that do present tidal debris.

Type	Tidal Tails	Streams	Shells
MATLAS ETGs	0.28 (1.89)	0.28 (1.42)	0.44 (2.82)
CFIS ETGs	0.00 (–)	0.29 (1.0)	0.00 (–)
VESTIGE ETGs	0.38 (1.47)	0.16 (1.12)	0.30 (2.5)
Total ETGs	0.30 (1.74)	0.25 (1.35)	0.40 (2.76)
MATLAS LTGs	0.60 (2.0)	0.06 (1.0)	0.22 (1.48)
CFIS LTGs	0.50 (1.87)	0.27 (1.43)	0.14 (1.71)
VESTIGE LTGs	0.58 (1.65)	0.08 (1.67)	0.13 (1.42)
Total LTGs	0.55 (1.83)	0.16 (1.41)	0.15 (1.55)
Total	0.42 (1.79)	0.21 (1.37)	0.28 (2.28)

4 GLOBAL STATISTICAL RESULTS

4.1 Incidence of tidal features

The total fraction of galaxies in our sample showing any sign of interaction (i.e. one or more features of any type) is 36%. If we distinguish between the types of features, 23% of galaxies host tidal tails, 15% host streams and 12% host shells. We also counted the number of tidal features around each galaxy. To that end, we used the selection process described in Section 4.8 of Sola et al. (2022) for tidal tails and streams, i.e. for these feature types identified by several contributors around a galaxy, only the largest is kept at the end of the selection. A different process is needed for shells. Indeed, the selection is based on the percentage of intersection between features, yet shells are annotated using one pixel-wide lines so the intersection would be null. In addition, we are facing the issue of the precise delineation of shells, which depends on the expertise of the contributors. If a shell is ambiguous and not so bright, it can be drawn as a single long arc by an expert contributor, while it can be cut in several parts by a less-expert contributor. Hence we consider the mean number of shells per contributor and galaxy for the census of shells²¹. The mean number of tidal features per galaxy, detailed by survey and morphological type, can be found in Table 4.

Tidal tails are more numerous around LTGs than ETGs, with a mean number of 0.55 and 0.30 per galaxy, respectively, which is statistically significant according to the 2-sample KS-test (p-value = 0.04 so we can reject the null hypothesis that the samples come from the same distribution). There is no significant difference in the number of streams for ETGs and LTGs, in terms of means (p-value = 0.08 for the t-test) and distributions (p-value = 0.54 for the 2-sample KS-test). Although shells seem more numerous around ETGs than LTGs, this is not significant as the 2-sample KS-test revealed similar distributions (p-value of 0.46). The conditions of application of the t-test were not verified for the number of tails and streams.

The higher fraction of tails around LTGs than ETGs is mainly explained by contamination from ongoing tidal interactions, which is higher for LTGs than ETGs. Indeed, disk galaxies are more susceptible to producing distinct prominent antennae-like features, due to their low local velocity dispersion and thinness, while elliptical galaxies will trigger more diffuse plume-like tails (e.g., Duc & Renaud 2013). A similar fraction of streams observed around ETGs and LTGs was expected. Indeed, as streams originate from lower-mass

companions, the morphological type of the primary galaxy should not directly impact the companions. For shells, the important parameters for their formation are the impact parameters, and not so much the morphological type of the primary galaxy.

4.2 Luminosities of LSB features

The luminosity of haloes and tidal features, derived from the observed flux, is an important quantity to measure as it can be compared with that of simulated features. The flux was automatically retrieved through aperture photometry with the masks of the annotations, as described in Section 3.2.

We calculated the fraction of the total flux emitted by the tidal features and haloes in each system. For each galaxy, we summed the flux in all the tidal features (tails and streams), and we divided it by the flux of the entire galaxy annotation, including both the inner galaxy and the extended LSB stellar halo. This luminosity fraction of tidal features $f_{L, \text{tidal}}$ is presented in the left panel of Figure 2 for only the galaxies that display tidal features. This section showed that 64% of the sample galaxies do not display tidal features, i.e., $f_{L, \text{tidal}} = 0$; the median value is also zero. Therefore we represent the means of the distributions instead of the medians. The same exercise was performed for haloes: we retrieved the flux in the extended LSB stellar halo (i.e., the faint outskirts that do not include the inner galaxy) and divided it by the total flux of the galaxy. Unlike tidal features, all galaxies have a halo (when the annotation is possible), hence the median value can be represented instead of the mean. The luminosity fraction of haloes $f_{L, \text{halo}}$ is presented on the right panel of Figure 2.

The mean luminosity fraction in both tails and streams is 3.6% (3.7% for tails only and 2.1% for streams only). The distributions are dominated by very low $f_{L, \text{tidal}}$, as the median values for tails and streams are 1.8%, against 1.9% for tails and 0.7% for streams. The median fraction of luminosity is 13.4% for ETGs and 8.2% for LTGs.

Although most haloes have $f_{L, \text{halo}} < 22\%$, a few systems with large $f_{L, \text{halo}}$. However, they either correspond to very close and interacting pairs where it is impossible to distinguish the halo of the target galaxy and that of the companion, or to very large ellipticals (e.g., central galaxies in the Virgo cluster). A comparison to the literature will be presented in Section 9.1.

In addition, we present the median surface brightness in tails and streams in the bottom panel of Figure 2. Streams are fainter than tails, with a median surface brightness of 26.8 and 26.1 mag arcsec⁻², respectively, with Mood’s test confirming this difference to be statistically significant. The faintest stream reaches a median SB of 27.8 mag arcsec⁻², about one magnitude brighter than our SB limit.

5 TRENDS AS A FUNCTION OF THE MASS OF THE HOST GALAXY

In this section, we investigate the relationships between the incidence of tidal features, their luminosity, and the host galaxy’s mass. The computation of the stellar mass is presented in Appendix A. We then perform a similar analysis for haloes. As galaxies are spread over a wide range of masses (see Figure 1), it is necessary to group data into bins of mass containing approximately the same number of galaxies, i.e. different bin widths. In each bin, the mean or median values of the quantity of interest are computed, and represented on a scatter plot.

²¹ We assume here that our four contributors have similar levels of expertise.

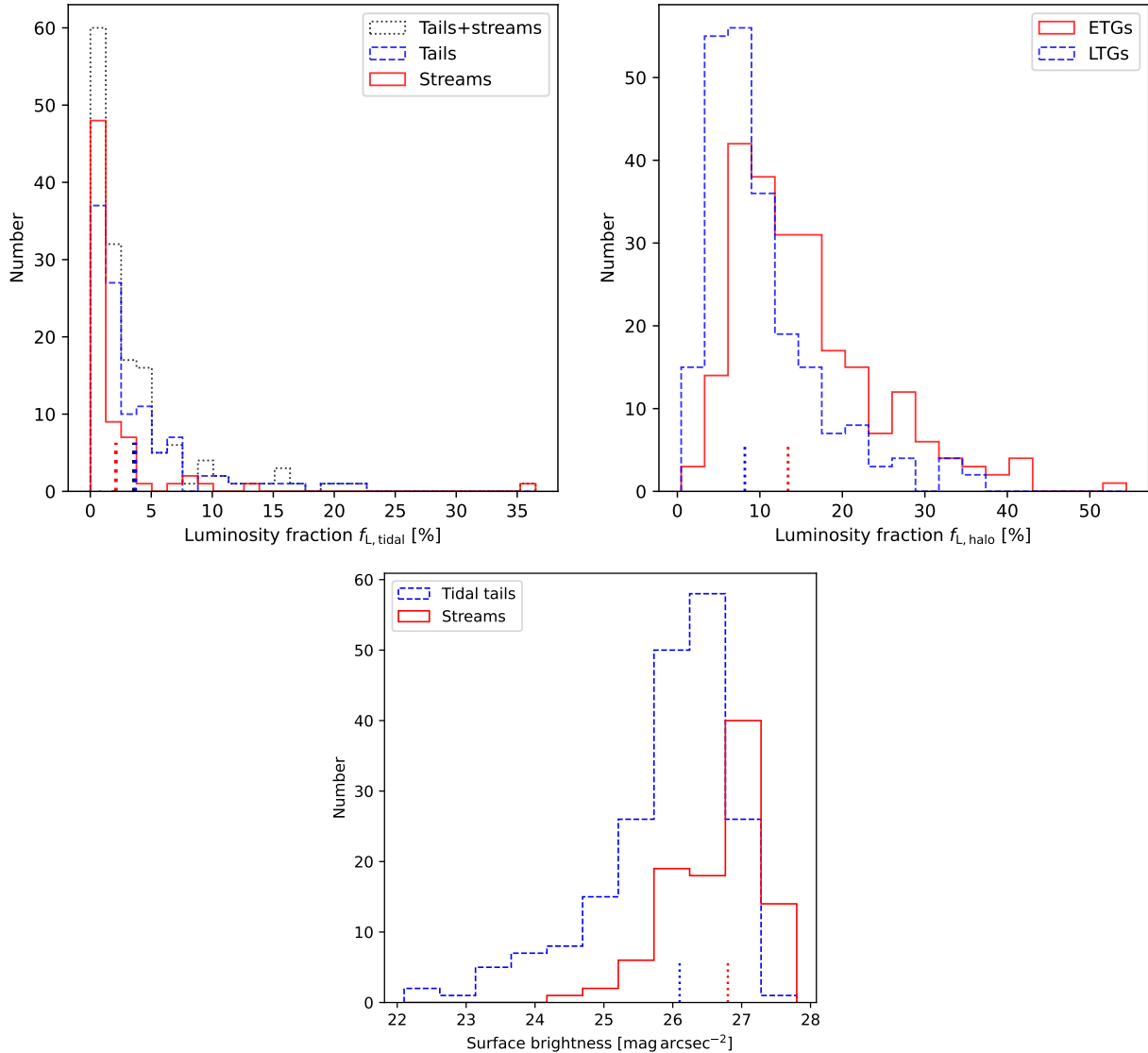


Figure 2. Histograms of the luminosity fractions in tidal tails and streams $f_{L,tidal}$ and haloes $f_{L,halo}$, and of the median surface brightness in tails and streams. *Top, left:* $f_{L,tidal}$ of tails (blue), streams (red) and tails and streams combined (black). The vertical dotted lines represent the mean values of the respective distributions. *Top, right:* $f_{L,halo}$ of ETGs (red) and LTGs (blue). *Bottom:* median surface brightness of tails (blue) and streams (red). The vertical dotted lines represent the median values of the respective distributions.

5.1 Tidal features

In the top panel of Figure 3, we study the evolution of the fraction of galaxies hosting tidal debris as a function of galaxy mass and show the results²². The fraction of galaxies hosting debris increases with galaxy mass for all types of tidal features. The fraction of galaxies with any type of debris is around 20-30% for galaxy masses lower than $3 \times 10^{10} M_{\odot}$, but it increases sharply up to 60% for the highest mass galaxies. This increase is statistically significant at a 5% confidence level, as Spearman’s test revealed a positive monotonic relation between both quantities (p-value of 0.02). This trend is driven by all

three types of tidal features, as the fraction of galaxies with tails goes from approximately 20% to 30%, from 5% to 22% for shells and from 12% to 25% for streams, with a sharper increase around the same mass threshold. When we separate the galaxies as a function of the morphological type, a similar global increase in mass is observed (see Figure 4). Tails primarily influence the trend for LTGs, whereas the steeper rise observed for ETGs is attributed to all types of tidal features.

To study the evolution of the luminosity fraction of tails and streams ($f_{L,tidal}$) as a function of galaxy mass, we divided our sample between low- and high-mass galaxies based on a mass threshold of $M > 4 \times 10^{10} M_{\odot}$. We also confirmed that the results from the statistical tests do not change if we take mass thresholds of 3, 5, 6, 7 or $8 \times 10^{10} M_{\odot}$. We compared $f_{L,tidal}$ in the low- versus high-mass samples. The t-test revealed similar means (p-value of 0.068), but the distributions and the median are statistically significantly differ-

²² The bottom panel of Figure 3 presents results that will be studied in Section 6.1, where we will separate features from ongoing interactions in pairs of galaxies (bottom right) and features around isolated galaxies (or ‘post-merger’) (bottom left). However, we consider in this section all galaxies together, whether interacting or isolated.

ent from the 2-sample KS-test and Mood’s test. Hence, more massive galaxies have slightly more luminous tidal features.

5.2 Haloes

Although tidal features are the most prominent signs of interactions, their lifetime is limited, and they will eventually phase-mix and contribute to the diffuse light of the extended stellar halo. Characterising the luminosities of haloes with galaxy mass will enable us to probe their assembly history over longer periods than with tidal features alone. In the hierarchical paradigm, haloes’ properties (e.g., mass, shape, density profile) are a function of the merger history (e.g., Purcell et al. 2007; Cooper et al. 2013; Pillepich et al. 2014; Elias et al. 2018), with a build-up through multiple interactions and merger events.

We investigated the evolution of the luminosity fraction in haloes as a function of galaxy mass, as presented in Figure 5. The median percentage of $f_{L,halo}$ per mass bin is represented in red for ETGs and in blue for LTGs. For ETGs, there is an increase of $f_{L,halo}$ with mass, from around 12% to 28% in the highest mass bin. This increase is more noteworthy for masses higher than about $5 \times 10^{10} M_{\odot}$, and Spearman’s test revealed a statistically significant monotonic relation between $f_{L,halo,ETGs}$ and mass. For LTGs, the fraction remains roughly constant (around 8%) with galaxy mass and no statistically significant correlation was found.

6 TRENDS AS A FUNCTION OF THE ENVIRONMENT

In this section, we investigate the dependence between the environment and collisional debris and haloes. The environment can be parameterised in different ways. We distinguish between the large-scale environment (field, group, cluster) and the small-scale one (presence of a nearby companion susceptible to generating tidal interactions).

The large-scale environment is characterised by the density parameter ρ_{10} . In the following plots, galaxies are grouped in bins of environment density that contain approximately the same number of galaxies per bin. The small-scale environment was defined using the annotations made using *Jafar*. Contributors were asked to delineate a companion galaxy as a massive nearby galaxy if it was considered close enough to be able to trigger detectable tidal interactions. We set a threshold of a projected distance of 100 kpc²³. Note that we were not able to check the actual mass of the galaxy (except if it was a galaxy from the reference sample of ATLAS^{3D}); we estimated the galaxy as massive if its size was close to the one of the target galaxy, i.e. not a dwarf or a much smaller companion. In addition, galaxies can be close in projection but their actual distance can be larger, and we do not correct for this effect.

Galaxies with no such companion are referred to as ‘isolated’ or ‘post-merger’, while galaxies having at least one companion are termed ‘in pairs’. For clarity, even if the galaxy has several companions, it is referred to as in pairs. With this definition, a galaxy in the Virgo cluster can be considered isolated, and a galaxy in the field/group can be in a pair.

Separating on-going collisions (47% of the sample) and isolated galaxies is highly relevant for our study. Indeed, while the young tidal features produced in on-going interactions give information about the future of the host galaxy, and a possible imminent merger, only the

features from ancient mergers are able to trace the past mass assembly we wish to reconstruct.

6.1 Tidal features

We studied the evolution of the tidal features fraction and luminosity as a function of the large-scale environment. The 2-sample KS-test and Mood’s test revealed similar distributions and median values of $f_{L,tidal}$ in the field/group and the Virgo cluster. The potential difference between the mean $f_{L,tidal}$ (1.4% in the field/group and 0.65% in the cluster) could not be statistically tested because the conditions of application of the test were not verified. In addition, no statistical difference was found for the fraction of galaxies hosting debris, with 35% in the field/group and 37% in the Virgo cluster. However, several trends are visible when studying the evolution of this fraction as a function of the environmental density, as presented in the top panel of Figure 6.

The fraction of galaxies hosting debris (Figure 6) exhibits a first well-defined peak between $-2 < \log_{10}(\rho_{10}) < -1.5$; it rises from 25% to a maximum of 50%. It then decreases to 30% before reaching another maximum of 50% in the highest-density bin. This trend is driven mainly by tidal tails (rising from 10% to 40%). The first peak is present but less pronounced for galaxies with shells or streams, and their fraction then diminishes at higher galaxy densities²⁴.

The decrease of debris incidence in the lowest environment density bin (about 25%) was expected, as there are fewer close-by galaxies to interact with. The small-scale environment – on-going collisions generating tidal tails – explains the two peaks observed in galaxy densities typical of groups and clusters. As shown in the bottom panels of Figure 6, isolated galaxies do not show any prominent peak for the incidence of tidal features. Similar conclusions hold when considering separately ETGs from LTGs (Figures D1 and D2). The plateau in the debris incidence at intermediate densities can be related to the influence of the positions of the galaxies inside the cluster, which will be discussed in Section 9.1.2 and in Appendix G.

This result motivated us to re-analyse the evolution of galaxies with debris as a function of galaxy mass taking into account the small-scale environment. These fractions are presented on the bottom panel of Figure 3. The trend we report in Section 5.1 – an increase in the fraction of galaxies with debris with galaxy mass – remains valid both for isolated and galaxies in pairs. For isolated galaxies, this fraction ranges between 19% and 55% (overall of 31%), while for galaxies in pairs, it ranges between 27% and 67% (overall of 42%). The overall fractions are statistically different (from the Z-test, with a p-value of 0.016). This increase is mostly driven by tidal tails, with a higher fraction of galaxies with tails among the ones in pairs. No statistically significant difference between isolated and galaxies in pairs is found for streams and shells. The global increase of galaxies hosting debris as a function of galaxy mass is also seen when separating ETGs from LTGs (Figure D3), with steeper slopes above a mass threshold around $1 - 3 \times 10^{10} M_{\odot}$.

This analysis confirms, for our SB limit, that the fraction of real post-merger galaxies with debris increases significantly with galaxy mass. Therefore in the recent history (up to a few Gyr), the most massive galaxies in our sample have undergone more merger events.

²³ This arbitrary threshold is low enough to ensure that any tidal interaction would trigger detectable tidal features.

²⁴ We have tested the influence of the binning, and at a 1σ level, the value of the incidence of debris around $\log_{10}(\rho_{10}) = -2$ is always higher (not within the error bars) than the incidence in the lowest-density environment bin. The plateau at intermediate densities is also always visible.

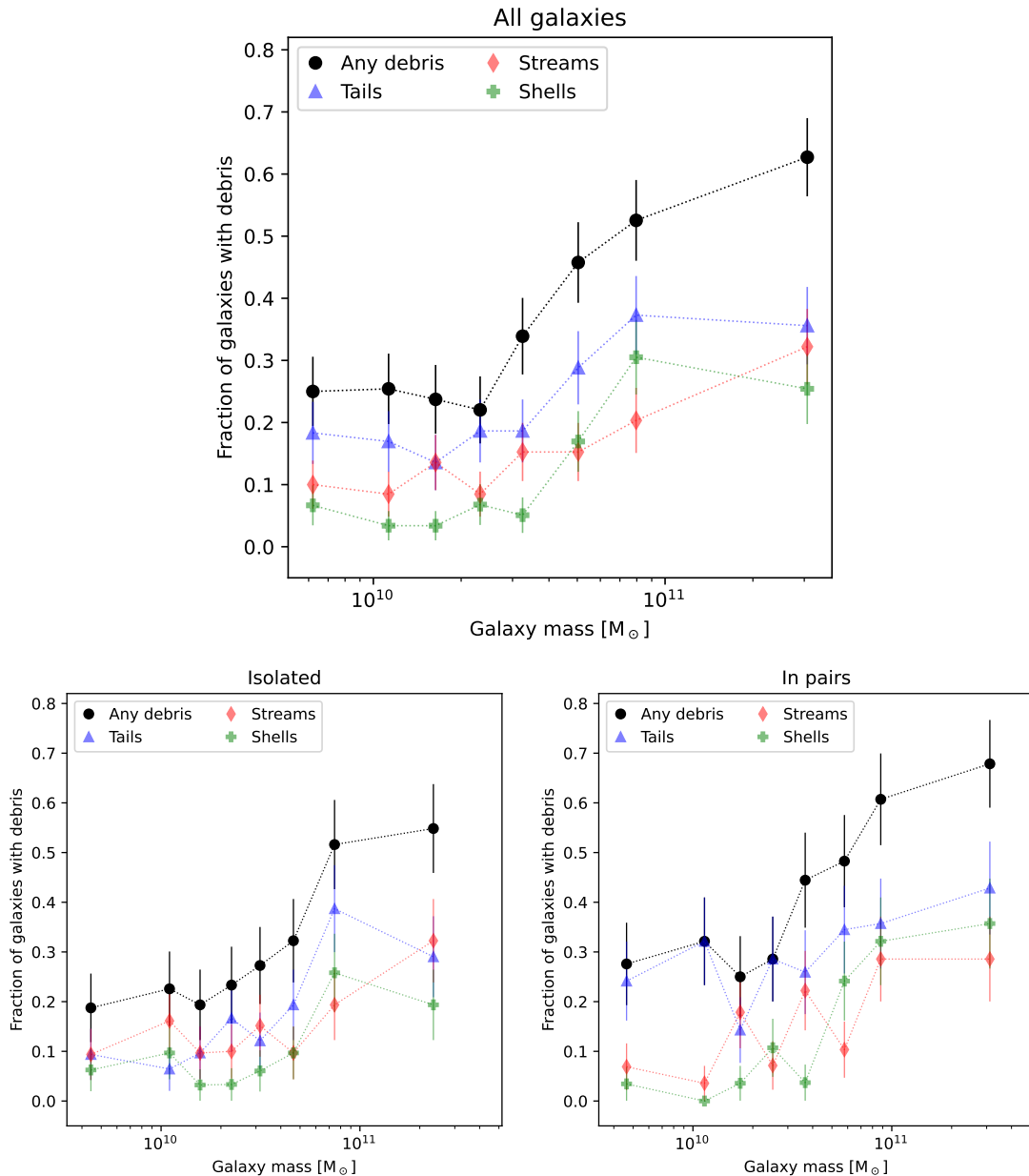


Figure 3. Fraction of galaxies that have tidal features as a function of the galaxy stellar mass (in M_{\odot}), per mass bin. Each bin contains approximately the same number of galaxies (i.e. about 60 galaxies per bin for the top panel, about 31 for the bottom left and 28 for the bottom right). The fraction of galaxies hosting any type of debris is plotted in black, galaxies hosting tails in blue, streams in red and shells in green. The error bars represent the standard deviation on proportions in each bin. *Top:* Fraction of galaxies with debris considering all galaxies together. *Bottom left:* Fraction of galaxies with debris only considering isolated (i.e. post-merger) galaxies (see Section 6.1). *Bottom right:* Fraction of galaxies with debris only considering galaxies in pairs, i.e. that can be undergoing tidal interactions with a massive companion.

However, it must be noted that tidal tails can also originate from non-merging flybys (e.g., Gnedin 2003; Sinha & Holley-Bockelmann 2012; Mosenkov et al. 2020).

6.2 Haloes

In this section, we investigate the impact of the environment on the relative luminosities of the LSB stellar haloes. Note that we do not disentangle between the halo light and the intracluster light, so we are likely overestimating the intrinsic halo luminosity in the Virgo

cluster. Figure 7 presents the evolution of the halo luminosity fraction $f_{L,\text{halo}}$ as a function of the environment density.

The overall median $f_{L,\text{halo}}$ of ETGs (resp. LTGs) equals 13.7% (resp. 7.6%) in the group/field and 13.1% (resp. 11.3%) in the Virgo cluster. There is no statistically significant relation for $f_{L,\text{halo}}$ versus ρ_{10} for ETGs, but it is significant (p-value = 2×10^{-4} for Spearman's test) for LTGs.

The increase of $f_{L,\text{halo}}$ with ρ_{10} , only visible for LTGs, suggests an effect of the environment, in particular ram-pressure that removes gas and then quenches star-formation in dense environments, in par-

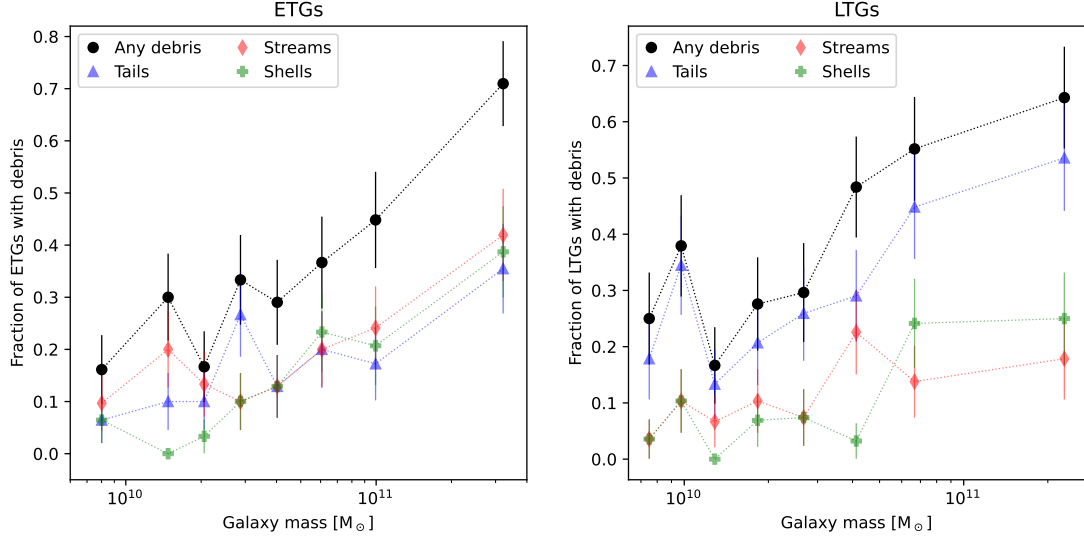


Figure 4. Fraction of ETGs (*left*) and LTGs (*right*) that have tidal features as a function of the galaxy stellar mass (in M_{\odot}), per mass bin. Each bin contains approximately the same number of galaxies, i.e. about 30 galaxies per bin in the left plot and 29 in the right plot. The fraction of galaxies hosting any type of debris is plotted in black, galaxies hosting tails, in blue, streams in red and shells in green. The error bars represent the standard deviation on proportions in each bin.

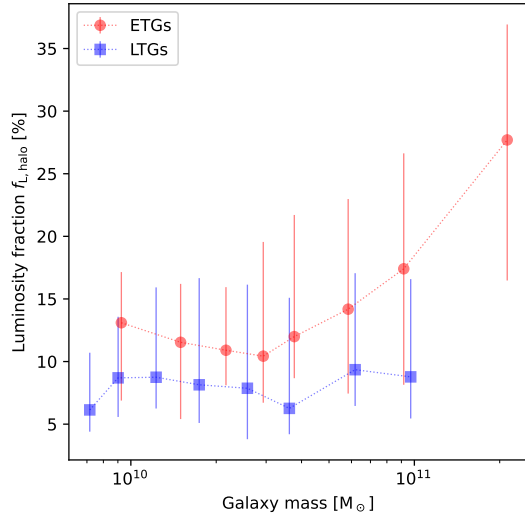


Figure 5. Scatter plot of the median fraction of luminosity of the haloes $f_{L,halo}$ as a function of the galaxy mass (in M_{\odot}). Each bin contains approximately the same number of galaxies; i.e. about 29 galaxies per bin for ETGs and 28 for LTGs. Large solid markers indicate the median values in each mass bin: red circles for ETGs and blue squares for LTGs. The lower (resp. upper) error bars represent the 16% (resp. 84%) quantiles in each bin.

ticular clusters. Since the pioneering work of [Gunn & Gott \(1972\)](#), many studies have demonstrated that ram-pressure stripping has an important impact on the evolution of spiral galaxies (see, e.g., [Boselli et al. 2022](#), for a recent review). Ram-pressure stripping removes the gaseous component, leading to gas disc truncation. Star formation is then reduced or even stopped, first in the outer disc/halo, making it redder in comparison to the bluer galaxy center ([Boselli et al. 2006](#)). Ram-pressure stripping should not directly alter the stellar disc ([Boselli et al. 2022](#)). On the contrary, galaxy harassment can trigger truncations both in the gaseous and stellar discs, but it could

also trigger nuclear star formation or AGN activity (e.g., [Henriksen & Byrd 1996](#); [Mastropietro et al. 2005](#)).

A deficit of atomic hydrogen (HI) may trace the presence of ram-pressure. We quantified the gas depletion by comparing the observed HI mass of cluster galaxies and the expected HI mass of field galaxies of similar morphologies and sizes, known as the HI-deficiency. HI-deficient galaxies have smaller HI discs²⁵ than their field counterparts ([Cayatte et al. 1990](#)) as well as smaller star forming disks, and therefore proportionally larger red discs/haloes (e.g., [Koopmann & Kenney 2004](#); [Boselli & Gavazzi 2006](#); [Fossati et al. 2013](#)). Figure 8 illustrates this process with a sequence of HI maps available for a select few Virgo galaxies ([Chung et al. 2009](#)) superimposed on NGVS images. From left to right, the extent of the HI disc (i.e., the ability to form stars) covers smaller and smaller regions up to the point where almost no gas is left.

The relations between truncated discs and ram-pressure stripping in the Virgo cluster had already been studied extensively (see e.g., Figure 9 of [Boselli et al. 2022](#)). HI-deficient galaxies show signs of outside-in stripping, as the gaseous discs are reduced with respect to the stellar discs.

Here, our goal was to determine whether the sole visual inspection of the extent of the stellar halo compared to star-forming regions in deep images using *Jafar* would be enough to give hints of ram-pressure stripping, without any information on the gas content. To that end, we computed the ratio between the areas of the manually annotated quenched *Halo* and star-forming *Inner galaxy*. This relative size of Virgo star-forming discs was compared to HI-deficiency values from Table 3 of [Chung et al. \(2009\)](#), which were available for 27 of our LTGs in Virgo. The results are presented in Figure 9. Although there is a large scatter due to the small sample size, the relative size of the quenched stellar halo seems to increase with increasing HI-deficiency, which can be seen as a hint of outside-in star-formation quenching for LTGs in the Virgo cluster.

A complementary visual inspection of the true colour images re-

²⁵ The size of the HI disk depends on the depth of the HI observation.

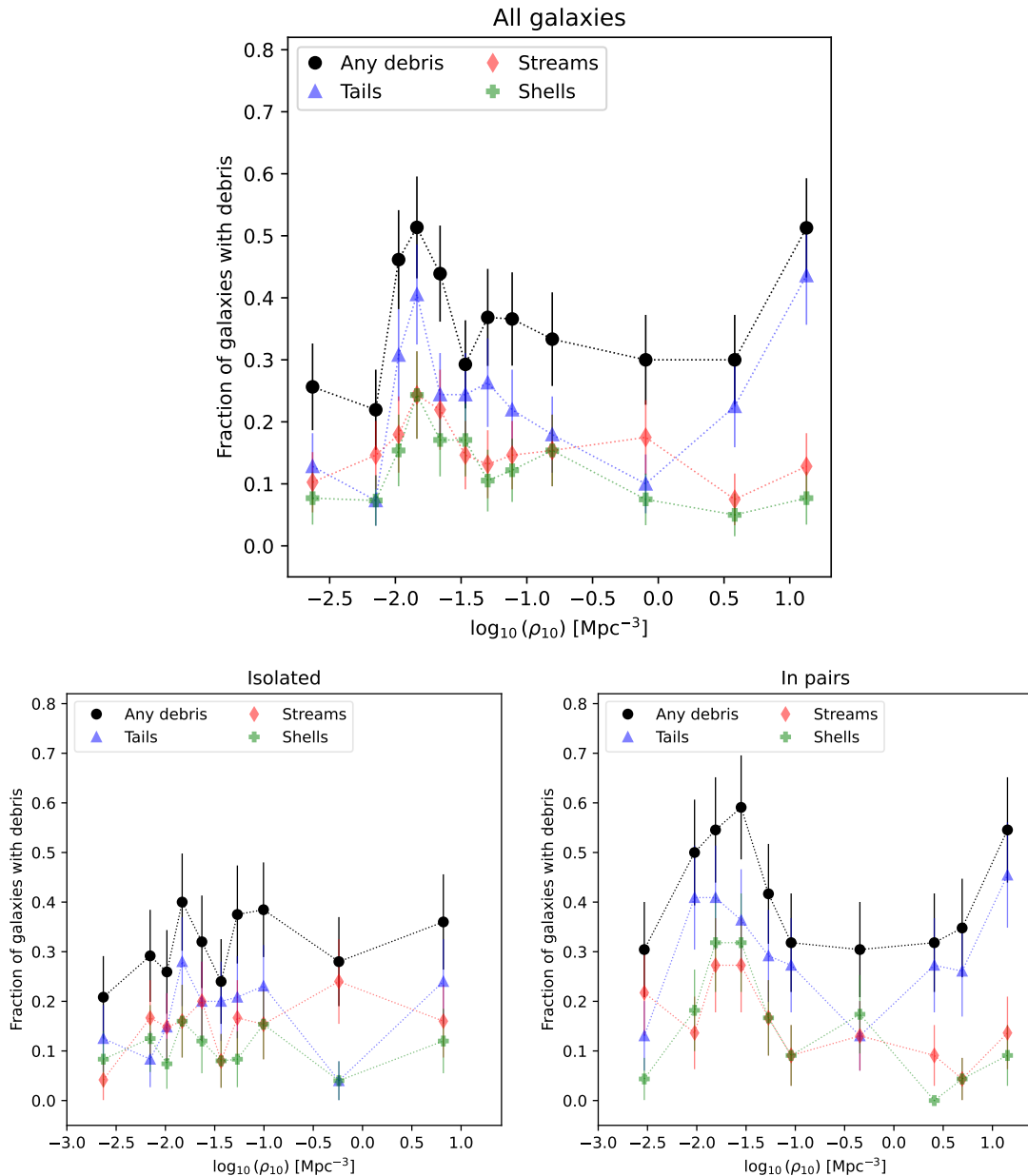


Figure 6. Fraction of galaxies that have tidal features as a function of the environmental density ρ_{10} (in Mpc^{-3}), per bin of ρ_{10} . Each bin contains approximately the same number of galaxies (i.e. about 39 galaxies per bin for the top panel, 25 for the bottom left panel and 22 for the bottom right panel). The fraction of galaxies hosting any type of debris is plotted in black, tails in blue, streams in red and shells in green. The error bars represent the standard deviation in each bin. Galaxies in the Virgo cluster have $\log_{10}(\rho_{10}) > -0.4$. *Top*: Fraction of galaxies with debris considering all galaxies together. *Bottom left*: Fraction of galaxies with debris only considering isolated (i.e. post-merger) galaxies). *Bottom right*: Fraction of galaxies with debris only considering galaxies in pairs (i.e. that could be undergoing tidal interactions with a massive companion).

vealed for some galaxies clear signs of on-going ram-pressure stripping, such as blue clumps oriented along small filaments perpendicular to the morphological major axis of the galaxy, that resembled smaller versions of jellyfish galaxies (e.g., Bekki 2009; Poggianti et al. 2016; Durret et al. 2021). These galaxies are indicated as black crosses in Figure 9.

To conclude, while the large-scale global environment does not seem to significantly impact the estimated size of massive galaxies, a small trend is observed for LTGs in the densest environment, possibly due to a ram-pressure effect.

7 THE COMBINED IMPACT OF MASS AND ENVIRONMENT

In the previous sections, we studied the effect of galaxy mass and environment on the incidence and importance of the LSB stellar structures around galaxies separately. However, it may be argued that mass and environment are correlated, with more massive galaxies residing in denser environments. We illustrate this possible dependence in Figure 10, which presents 2D-histograms showing the fraction of galaxies with debris and $f_{\text{L,halo}}$ as functions of the mass and en-

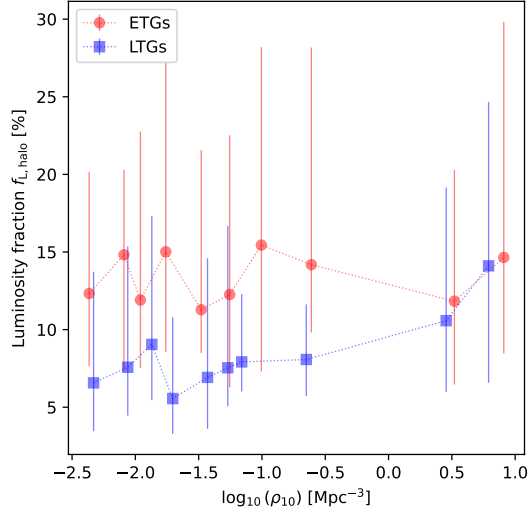


Figure 7. Scatter plot of the median fraction of luminosity of the haloes $f_{L,halo}$ as a function of the environment density ρ_{10} (in Mpc^{-3}). Each bin contains approximately the same number of galaxies; i.e. about 23 for ETGs and 22 for LTGs. Large solid markers indicate the median values in each bin of ρ_{10} , in red circles for ETGs and blue squares for LTGs. The lower (resp. upper) error bars represent the 16% (resp. 84%) quantiles in each bin. Galaxies in the Virgo cluster typically have $\log_{10}(\rho_{10}) > -0.4$.

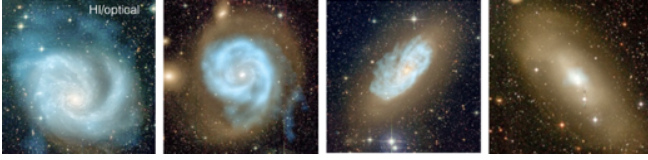


Figure 8. Illustration of a ram-pressure stripping sequence for LTGs in the Virgo cluster. VLA HI maps (Chung et al. 2009) are superimposed in blue on NGVS u,g,r true color images.

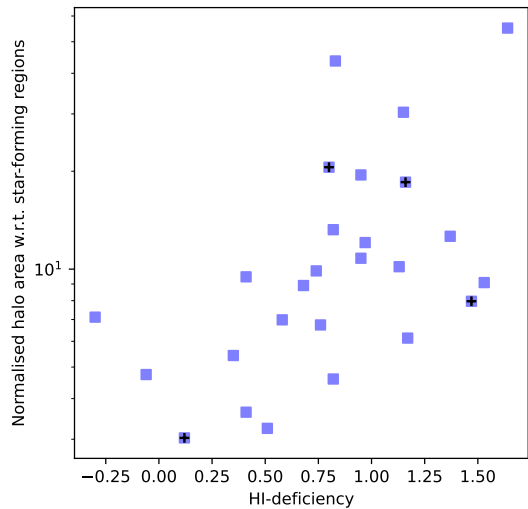


Figure 9. Scatter plot of the area of the quenched *Halo* annotation normalised by the area of star-forming *Inner galaxy* annotation, as a function of the HI-deficiency for LTGs in the Virgo cluster with available HI-deficiency values from Chung et al. (2009). Galaxies which show hints of extra-planar star-forming regions in stripped HI gas are indicated with black crosses

vironment simultaneously. The 2D-bins were computed to contain approximately the same number of galaxies.

There is no evolution with ρ_{10} except in the highest mass bin for the fraction of galaxies with debris at fixed mass. At fixed ρ_{10} , there is a trend with galaxy mass for all environment density bins. Hence, this fraction increases more with galaxy mass than the environment density. A similar trend is found for the luminosity fraction in haloes, although the highest value of $f_{L,halo}$ is reached in the 2D-bin with the highest environment density and mass. Since the strongest correlations are found between both parameters and the mass, our approach of studying the effect of mass and environment separately seems justified.

8 TRENDS AS A FUNCTION OF THE INTERNAL KINEMATICS OF THE HOST GALAXY

In previous sections, galaxy morphologies were used to separate our sample between ETGs and LTGs. However, other classification schemes exist, such as internal stellar kinematics, which may be a more robust and fundamental parameter to distinguish the various types of galaxies. Most ETGs show regular rotation patterns (fast rotators, FRs) while others do not show any sign of rotation or complex kinematic features (slow rotators, SRs) (e.g., Emsellem et al. 2007, 2011). Separating SRs from FRs is essential when studying the evolution of ETGs, as a number of numerical simulations predict that ETGs should initially form as FRs and later transform into SRs through mergers (e.g., Naab et al. 2014; Penoyre et al. 2017; Lagos et al. 2018, 2022). Bílek et al. (2023) combined kinematic information from the ATLAS^{3D} sample of ETGs and merger-sensitive features (such as tidal features, kinematically distinct cores, stellar ages) to study the role of mergers in the transformation of FRs into SRs for the MATLAS sample (Duc et al. 2015; Bílek et al. 2020). According to their work, internal kinematics was implemented early (around $z = 2$) through multiple minor wet mergers.

Here, we extend the work of Bílek et al. (2023) (and previous works from the ATLAS^{3D} collaboration, e.g., Duc et al. 2011), and investigate the relationship between kinematics and the late assembly history of ETGs. We adopt a quantitative approach to the topic, and further probe denser environments by including ETGs in the Virgo cluster.

Following Emsellem et al. (2011) and Bílek et al. (2023), we based our analysis on the estimated rotational support, $\lambda_{R_e}^N = \lambda/\sqrt{\epsilon}$, where λ quantifies the degree of ordered rotation of the galaxy and ϵ the apparent ellipticity. This also includes 2- σ galaxies, which are characterised by two off-centre, but symmetric, peaks in the velocity dispersion, which lie on the major-axis of the galaxy (Krajnović et al. 2011). $\lambda_{R_e}^N$ is measured within one effective radius R_e . Galaxies with $\lambda_{R_e}^N < 0.31$ (resp. > 0.31) are considered SRs (resp. FR). With such a definition, 15% of our ETGs are SRs. From the 2-sample KS-test and Mood’s test, SRs in our sample are statistically significantly more massive than FRs. The distribution of our ETGs in the plane $\lambda_{R_e}^N$ versus environment density is shown in Figure 11. ETGs in our sample are preferentially located in the group environment (median $\log_{10}(\rho_{10}) = -1.4$) with a relatively high rotational support (median $\lambda_{R_e}^N = 0.76$).

8.1 Tidal features

We display the fraction of ETGs hosting debris as a function of the rotational support, $\lambda_{R_e}^N$, in Figure 12. Globally, when considering all

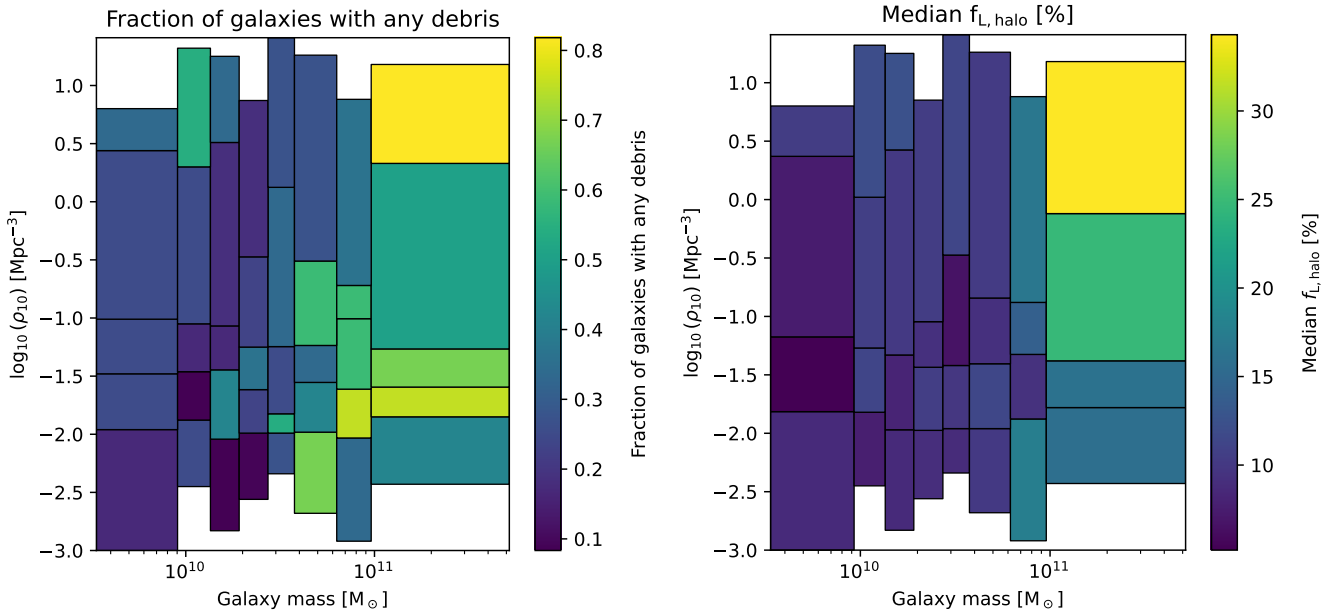


Figure 10. 2D-histograms of the fraction of galaxies hosting tidal features (*left*) and median fraction of luminosity in haloes $f_{L,halo}$ (*right*), as a function of the galaxy mass (in M_{\odot}) and environment density ρ_{10} (in Mpc^{-3}). Each 2D-bin contains approximately the same number of galaxies (i.e. 12 galaxies per 2D-bin for the left plot and 14 for the right plot).

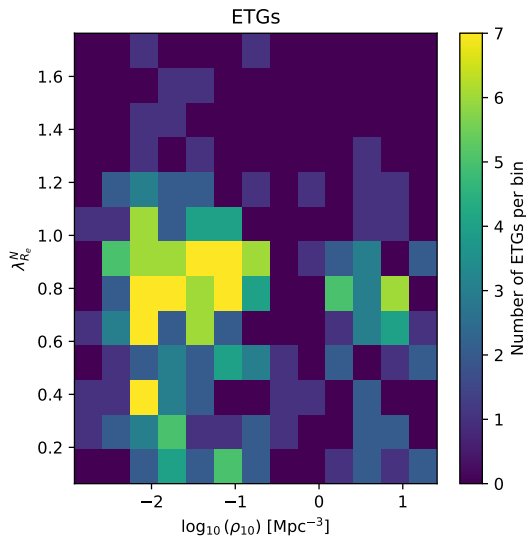


Figure 11. 2D histogram of the distribution of the number of ETGs as a function of the rotational support, λ_{Rc}^N , and of the environment density, ρ_{10} , in Mpc^{-3} . Galaxies in the Virgo cluster have $\log_{10}(\rho_{10}) > -0.4$. Galaxies with $\lambda_{Rc}^N < 0.31$ (resp. > 0.31) are considered SRs (resp. FR).

SRs versus all FRs, 42% of SRs host tidal debris against 33% for FRs, a difference which is not statistically significant according to the Z-test. However if we separate galaxies in Virgo versus in the field/group, a decrease in the fraction of galaxies with tidal features with λ_{Rc}^N is especially clear for Virgo ETGs. In addition, galaxies around $0.7 < \lambda_{Rc}^N < 1$ tend to have a higher fraction of tidal debris, a trend best visible in low galaxy density environments. As ETGs with this range of λ_{Rc}^N are preferentially located in the group environment (as seen in Figure 11), this increase could be triggered by multiple

interactions within the group, similar to the one observed in Figure 6.

In the top panel of Figure 13, we investigated whether we could separate the effect of mass and environment from internal kinematics through 2D histograms. Indeed, slow rotators are statistically more massive than fast rotators (e.g., Khochfar et al. 2011). For the fraction of ETGs hosting debris, there is a correlation with mass, but the trend with λ_{Rc}^N is less clear, in part because of our low number of SRs. The trends between environment density and λ_{Rc}^N seem less clear, with higher fractions of ETGs with debris for lower values of ordered rotation. A proper disentangling between the effect of the mass, environment and internal kinematics would require a study of the correlations at fixed mass and environment density, such as the one carried out by Blek et al. (2023). They found that the trends of tidal features stopped being statistically significant after accounting for the effect of mass. They concluded that the kinematic state was established at a high redshift, but the SRs keep experiencing more mergers until today.

8.2 Haloes

Figure 14 investigates the evolution of the luminosity fraction in haloes, $f_{L,halo}$, as a function of the rotational support, λ_{Rc}^N . A decrease of $f_{L,halo}$ with increasing λ_{Rc}^N is observed. Haloes of SRs (with a median $f_{L,halo} = 23\%$) are almost twice as luminous as those of FRs ($f_{L,halo} = 12\%$), which is a statistically significant difference. The origin of this trend could be due to galaxy mass; as seen in Figure 5, the most massive ETGs, preferentially SRs, have haloes almost twice as luminous as the low-mass ones.

The increase of $f_{L,halo}$ with lower rotational support values is also consistent with the picture of FRs transforming into SRs through old mergers that built the stellar haloes. Note that whereas tidal debris traces recent mergers younger than a few Gyrs, the extended

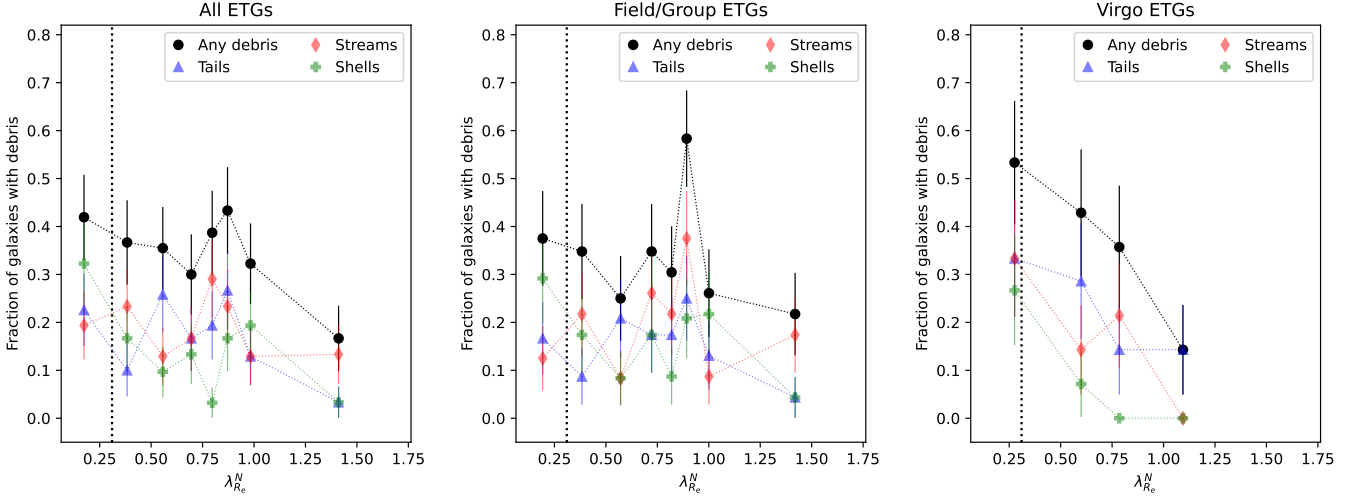


Figure 12. Scatter plot of the fraction of galaxies that have tidal features as a function of the rotational support, $\lambda_{R_e}^N$. Each bin contains approximately the same number of galaxies (i.e. 30 galaxies per bin for the left plot, 23 for the middle plot and 14 for the right plot). The fraction of galaxies hosting any type of debris is plotted in black, tails in blue, streams in red and shells in green. The error bars represent the standard deviation in each bin. The vertical dotted line separates SRs from FRs. Such fractions are presented for all ETGs (*left*), field/group ETGs (*middle*) and Virgo ETGs (*right*).

LSB haloes provides information on assembly events that might have occurred much earlier.

As seen in the bottom panel of Figure 13, $f_{L,halo}$ seems to correlate with mass, especially for slow rotators. Likewise, a correlation appears between $f_{L,halo}$ and $\lambda_{R_e}^N$ for slow rotators, while no trend is visible as a function of the environment except for slow rotators. Therefore, the degree of ordered rotation is more important than the environment for haloes.

9 DISCUSSION

9.1 Comparison to the literature

9.1.1 Incidence and luminosity of LSB features

All our results are reported for a SB limit of ~ 29 mag arcsec $^{-2}$. In Section 4.1 we found that 36% of our galaxies host tidal features (23% host tails, 15% host streams and 12% host shells). A direct comparison to the literature is not straightforward. The properties of the galaxies (e.g., distances, prominence of the tidal features) and properties of the studies (e.g., definitions of the types of tidal features, surface brightness limits, detection methods, image processing techniques, sample selection) differ from one study to the other (e.g., Atkinson et al. 2013; Hood et al. 2018).

This results in large discrepancies in the reported fraction of tidal features in nearby galaxies ranging from a few percent up to 70% (e.g., Malin & Carter 1983; Schweizer & Seitzer 1988; van Dokkum 2005; Tal et al. 2009; Bridge et al. 2010; Nair & Abraham 2010; Kaviraj 2010; Miskolczi et al. 2011; Kim et al. 2012; Sheen et al. 2012; Adams et al. 2012; Atkinson et al. 2013; Duc et al. 2015; Hood et al. 2018; Bílek et al. 2020; Jackson et al. 2021; Vázquez-Mata et al. 2022; Yoon et al. 2023; Rutherford et al. 2024). On the simulation side, Pop et al. (2018) produced a census of shells in the Illustris simulation and found an incidence of 20-30% for shells, which is higher than our finding, but they did not apply any SB limit cut. Martin et al. (2022) also produced a census of tidal features in simulated deep images considering different depths. They found

fractions roughly similar to ours (between a few per cent and less than 20%) for an SB limit of 29 mag arcsec $^{-2}$.

Tails and streams account for 2-4% of the total galaxy luminosity (Section 4.2). Even though the definitions of tidal features differ (as mentioned above), similar numbers are found in the literature. Jackson et al. (2021) estimated the stellar material in the outskirts of their massive central galaxies, mostly in the form of tidal and merger features, represent a few per cent of the total stellar mass (8% outside $2R_e$, which likely includes a part of what we defined as halo). Huang & Fan (2022) found their $f_{L,tidal}$ lower than 1% for tidal features around their massive ETGs in HSC-SSP images. Their values are obtained by summing the flux in pixels belonging to tidal features identified from residual images which may underestimate the true values. In simulations, Martin et al. (2022) found that the flux in tidal features ranges from 1 to 10% for the most massive galaxies. Their values are higher as they retrieve all the particles associated to a feature since the ground truth and the fraction of stars from accreted origin is known.

As observed in Sola et al. (2022), we find that streams are fainter than tails by 0.7 mag. The brightest tails are associated to on-going interactions, as tails around galaxies in pairs have a brighter median SB than tails around isolated galaxies (26.0 and 26.3 mag arcsec $^{-2}$ respectively). Even amongst isolated galaxies, streams remain fainter and this may be related to different survival lifetimes (e.g., Mihos 1995; Ji et al. 2014; Mancillas et al. 2019), with streams tending to remain visible longer than tails. No features are observed below 27.8 mag arcsec $^{-2}$ which is about 1 mag brighter than the SB limit. This is related to the difference in the measure of the SB limit (in $10 \times 10''$ boxes) and the SB of the extended, diffuse tidal features that display brightness fluctuations, as well as the fact that the annotation has been done visually and the eye is not able to detect the faintest structures. In addition, we report the median values, but some parts of the tidal features are fainter than others. This difference must be considered when comparing observations to simulations.

A word of caution must be added about our measurement of the luminosity in the haloes. We estimated it in a consistent way for all our galaxies (see Section 3.1) to enable comparisons and investigate

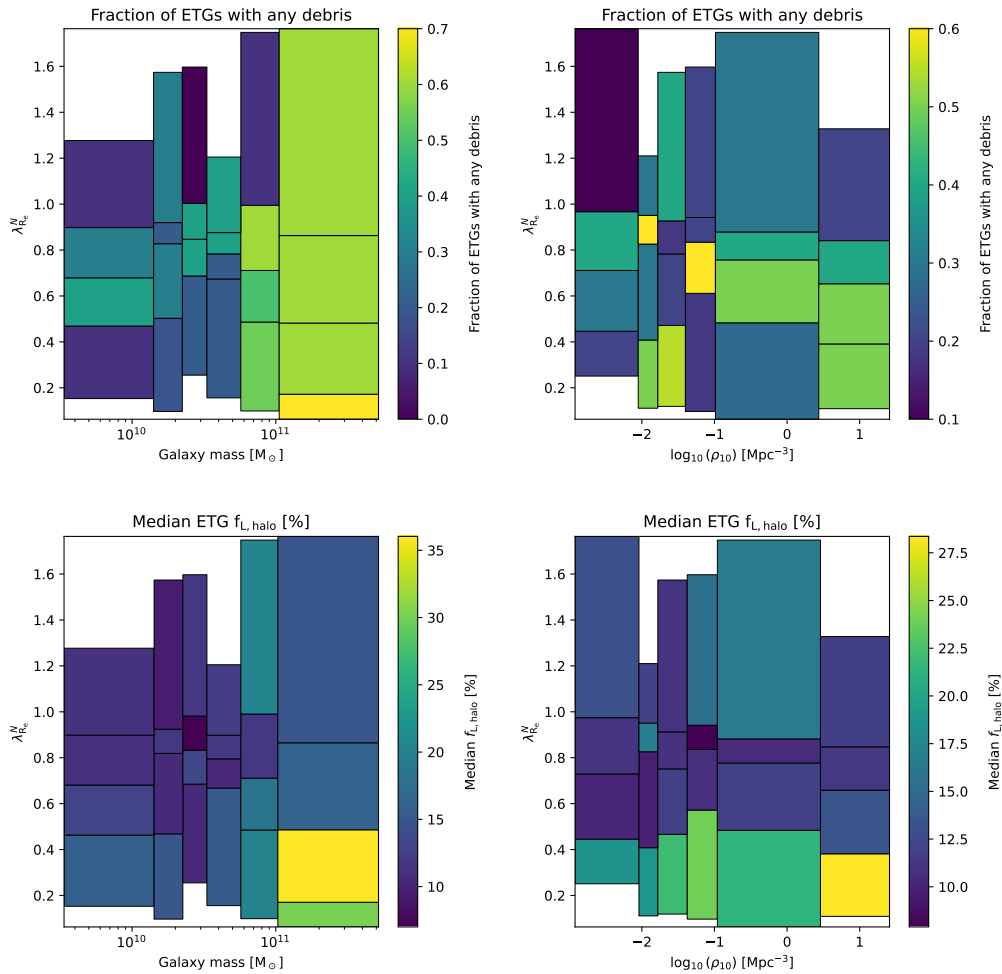


Figure 13. *Top row:* 2D-histograms of the fraction of ETGs hosting tidal features as a function of the degree of ordered rotation, λ_{Re}^N , and the galaxy mass (*left*, in M_{\odot}) and the environment density, ρ_{10} , (*right*, in Mpc^{-3}). *Bottom row:* 2D-histograms of the median luminosity fraction in haloes of ETGs, $f_{\text{L,halo}}$, as a function of the degree of ordered rotation, λ_{Re}^N , and the galaxy mass (*left*, in M_{\odot}) and the environment density, ρ_{10} , (*right*, in Mpc^{-3}). Each 2D-bin contains approximately the same number of galaxies (i.e. about 10 galaxies per 2D-bin for each plot). Galaxies with $\lambda_{\text{Re}}^N < 0.31$ (resp. > 0.31) are considered slow rotators (resp. fast rotators).

trends within our sample. One clear drawback of the method is that it does not allow a direct comparison with the literature. An accurate measurement would require deconvolving the image from the PSF (discussed in Section 9.2.2). In any case, a thorough comparison to the literature is not straightforward, as there is no unique definition of the halo and no way to measure it. For instance, Gilhuly et al. (2022) have investigated the variation of halo flux depending on four different definitions. The method is nevertheless precise enough to compare the relative importance of the stellar haloes.

The haloes in our sample account for about 13% of the total galaxy luminosity for ETGs and 8% for LTGs. Trujillo & Fliri (2016) found from the surface brightness profile that the halo of UGC00180 (having a stellar mass of $1.3 \times 10^{11} M_{\odot}$) represented 11% of the total flux in their original images (that had not been PSF-corrected). Likewise, using the ellipse-fitting method, Duc et al. (2015) calculated the flux below the 25 arcsec $^{-2}$ isophote for ETGs to be, on average, 4.5%, with a maximum of 14%. Gilhuly et al. (2022) estimated the halo fraction to range between less than one per cent and less than 7% using integrated light on twelve edge-on LTGs. However, their haloes are more extended than ours and hence the comparison is not

straightforward. Merritt et al. (2016) found a large range of values for the halo fraction for the eight spiral galaxies they studied, ranging from no halo detection to around 4.5% for the halo fraction. However, they used a method to separate the halo light from the bulge and disk, while with our halo definition we likely overestimate the luminosity fraction. The definition of the halo has an important impact in the measured halo mass fraction (e.g.; Sanderson et al. 2018; Gilhuly et al. 2022; Wright et al. 2023) that can either lead to the presence or to the absence of a trend with galaxy mass. In addition, it is important to recall that in this paper, we do not account for the effect of the PSF, which some of the aforementioned studies do consider. We will discuss this effect in Section 9.2.2. However, overall, there seems to be an agreement between our values and the literature.

Finally, we briefly compared the luminosity fraction in haloes in observations and in a few mock images from numerical simulations using our method in Appendix H. Although there is halo-to-halo variability, the order of magnitude of luminosity fraction aligns well between observation and simulations, though a thorough analysis is beyond the scope of this work.

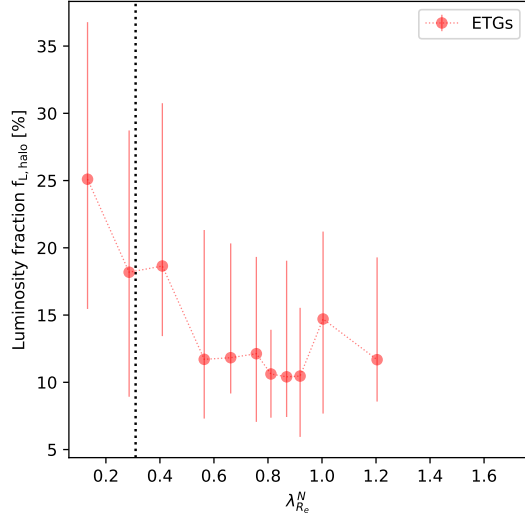


Figure 14. Scatter plot of the median fraction of luminosity in the annotated haloes of ETGs $f_{L,halo}$ (in %) as a function of the rotational parameter $\lambda_{R_c}^N$. Each bin contains approximately the same number of galaxies; i.e. 21. The lower (resp. upper) error bars represent the 16% (resp. 84%) quantiles in each bin. The vertical dotted line separates SRs from FRs.

9.1.2 The combined effect of mass and environment

As presented in Sections 5, 6 and 7, galaxy mass is the dominant effect that impacts the frequency of tidal features and relative luminosities of the haloes, a result also highlighted in previous publications. For instance, Atkinson et al. (2013) noted a mass-dependency, with an increased fraction of galaxies having tidal features (linear features, shells and fans of stellar light) for galaxy masses $> 10^{10.5} = 3.16 \times 10^{10} M_{\odot}$, which is very close to the mass threshold (i.e., a sharp increase of some properties above a given stellar mass) we observe. Likewise, Duc et al. (2015) and Bílek et al. (2020) reported an increased fraction of ETGs with shells, streams and disturbed isophotes with increasing galaxy mass, mostly for galaxies with a mass $> 10^{11} M_{\odot}$. Other studies, such as Yoon & Lim (2020), find a strong correlation between the fraction of ETGs with features and increasing galaxy mass: 30-40% of their massive ($M_{\text{dyn}} > 10^{11.4} M_{\odot}$) galaxies have tidal features, while 2-5% of their less massive ($M_{\text{dyn}} < 10^{10.4} M_{\odot}$) ETGs show features. Similarly, Vázquez-Mata et al. (2022) found the fraction of galaxies with any type of debris to increase with stellar mass, from 10% to 30% for their most massive galaxies.

On the simulation side, Martin et al. (2022) also noted a slight increase in the fraction of galaxies with shells, streams or tails with galaxy mass for an SB limit of 29 mag arcsec $^{-2}$. In four different numerical simulations, Khalid et al. (2024) found a similar increase of galaxies hosting tails and streams with stellar mass, ranging from a few per cent to about 20% for stellar masses around $10^{10} M_{\odot}$. Huang & Fan (2022) noted an increase in the fraction of flux in tidal features, $f_{L,tidal}$, from 0.5% for stellar masses around $10^{11} M_{\odot}$ to 1% for masses higher than $10^{12} M_{\odot}$. Martin et al. (2022) reported a substantial increase in $f_{L,tidal}$ with galaxy mass, above a stellar mass threshold of $10^{10.1} M_{\odot}$.

The presence of such a mass threshold, above which the increase of the aforementioned quantities are steeper ($3 \times 10^{10} M_{\odot}$ for the fraction of galaxies with debris, $4 - 7 \times 10^{10} M_{\odot}$ for $f_{L,tidal}$ and $5 \times 10^{10} M_{\odot}$ for $f_{L,halo}$) has also been reported in the literature: between a few

10^{10} and $10^{11} M_{\odot}$ (e.g., Atkinson et al. 2013; Duc et al. 2015; Bílek et al. 2020; Yoon & Lim 2020; Martin et al. 2022; Vázquez-Mata et al. 2022; Huang & Fan 2022). A threshold of $10^{10.81} M_{\odot}$ has also been noted by Lim et al. (2023) through the census of the globular cluster (GC) distributions. They interpret this as high-mass galaxies having accreted their GC systems while lower-mass galaxies have formed them in situ.

This approximate mass threshold also coincides with the galaxy mass where merger events become the dominant factor of galactic growth according to numerical simulations (e.g., Stewart et al. 2008; Rodríguez-Gomez et al. 2015). Likewise, Kauffmann et al. (2003) noted a change in galaxy properties around $3 \times 10^{10} M_{\odot}$, which matches our findings, with lower-mass galaxies having young stellar populations, disc-like structures, and low surface mass densities. These findings are consistent with the idea that the mass growth of the most massive galaxies is dominated by mergers (e.g., Newman et al. 2012; Hilz et al. 2013; Robotham et al. 2014; Rodríguez-Gomez et al. 2016; Vulcani et al. 2016; Hill et al. 2017a,b; Nevin et al. 2023), as gas accretion may no longer be possible (due to too hot haloes that prevent the fresh infall of gas), hence the presence of more luminous extended haloes as well as increased fraction and luminosity of tidal features. Kereš et al. (2005) and Dekel & Birnboim (2006) noted that around a similar mass threshold, lower-mass galaxies are dominated by cold accretion (i.e., gas accreted from cold, dense intergalactic filaments) and higher-mass galaxies are dominated by hot accretion (i.e., gas shock-heated to high temperature that later cools). Unlike massive ETGs, LTGs tend to have a smoother accretion history, mostly through gas accretion (e.g., Sancisi et al. 2008; Bílek et al. 2023). Indeed, if the LTGs had undergone major mergers, they would eventually have turned into ETGs (although gas-rich mergers can sometimes produce a spiral remnant, e.g., Springel & Hernquist 2005); hence, the LTGs visible today should have had a relatively quiet evolution in the past few gigayears.

Furthermore, all our results are obtained for a given surface brightness limit of about 29 mag arcsec $^{-2}$. One may wonder whether the increase in the fraction of galaxies with debris with increasing mass (Figure 3) could be explained by the fact that less massive galaxies would have fainter hence non-detected tidal features, rather than by an effect of galaxy mass. Numerical simulations can help disentangle between both effects. Martin et al. (2022) investigated the detectability and fraction of flux in tidal features as a function of surface brightness limit and stellar mass. From their Figure 12, more massive galaxies have tidal features which are more easily detected. For an SB limit of 29 mag arcsec $^{-2}$, the less massive galaxies ($10^{9.5} - 10^{10} M_{\odot}$) have no detectable features, while for galaxies above $10^{10.5} M_{\odot}$ more than 20% of the area of features is detectable. Therefore, in our study the actual fraction of galaxies with debris should be higher for all mass ranges, not only for the less massive ones. In addition, Figure 8 of Martin et al. (2022) shows an increase in the fraction of flux in tidal features with stellar mass for all depths, although the normalisation and scatter of the relations strongly depend on depth. For an SB limit of 29 mag arcsec $^{-2}$, the flux in features increases from 0.04% for $5 \times 10^9 M_{\odot}$ galaxies up to 7% for $3.2 \times 10^{11} M_{\odot}$ ones. Martin et al. (2022) conclude that more massive galaxies have tidal features which are both more frequent and brighter (in flux). This conclusion aligns with our results and we conclude that these trends are mostly due to galaxy mass rather than depth.

In this paper, we report no strong influence of the large-scale environment on the incidence of tidal features (see Section 6.1), except in the group environment probed by our sample. A possible increase in the fraction of galaxies with tails and shells in the group environment was also seen by Bílek et al. (2020). Previous studies reported

decreasing fractions of shells in higher-density environments (e.g., Malin & Carter 1983), which was explained by the fact that shells originate mostly from radial mergers with low-velocity encounters (e.g., Quinn 1984), unlike the high-velocity encounters in clusters. Indeed, in massive clusters such as Virgo the velocity dispersion is high (about 1000 km s^{-1} Gunn & Gott 1972), thus gravitational interactions are short living phenomena (Boselli & Gavazzi 2006). The probability of producing tidal tails or other LSB features should be very low. Here, we do not see any statistically significant trend for shells and streams. However, there is a net increase in the fraction of galaxies with tails in the cluster (Figures 6, D1 and D2). This suggests that although tidal feature evaporation was expected in clusters, the Virgo cluster environment is not unfavourable to the formation of young tidal tails. It could also be possible that tidal features are rapidly destroyed but new ones could also form quickly, making the distinction between these competing processes complicated.

Another factor to consider is the location of the galaxies inside the cluster itself, as strong dependencies have been noted in the literature between the positions and some galaxy properties (e.g., Gnedin 2003; Mihos 2004; Boselli & Gavazzi 2006; Janowiecki et al. 2010; Adams et al. 2012; Boselli et al. 2014). We study the evolution of the fraction of galaxies with debris as a function of the clustercentric distance in Appendix G. The close proximity of companion galaxies, i.e. small-scale environment, seems responsible for the formation of tidal features, especially tails. These features may later be destroyed by competing processes in the cluster.

9.1.3 The effect of internal kinematics

In Section 8, we found increased fractions of SRs hosting shells compared to FRs, and increased values of halo luminosity fraction for ETGs with lower rotational support. Other works have investigated the links between tidal features and internal kinematics. For instance, Rutherford et al. (2024) used streams and tails around SRs and FRs in the SAMI Galaxy Survey using deep HSC data, in order to trace their dynamical evolution. Likewise, Yoon et al. (2024) studied the fraction of galaxies with tidal features as a function of the kinematics of 1244 ETGs. The higher fraction of shells around SRs than FRs was also reported by Rutherford et al. (2024). Similarly, Yoon et al. (2024) found that half of their ETGs with shells are SRs, and that ETGs with tidal features have reduced rotational support compared to ETGs without such features. They also found that ETGs with low λ_{Re}^N preferentially host shells compared to tails and streams, which is comparable to what we observed except in the group environment where this fractions can be increased due to close interactions.

About haloes, we interpreted the increase of the luminosity fraction for SRs as signs of old mergers. However, other effects than mergers act on haloes in clusters. The numerous, high-velocity flybys (e.g., Moore et al. 1996), particularly at near the cluster center, contribute to stretch the outer galactic material further away and lead to more extended haloes. In addition, Boselli et al. (2014) found for ETGs in the Virgo cluster that the most massive galaxies are SRs, and the lower-mass SRs preferentially located in the higher-density substructures of the cluster. They outline that the massive systems likely result from major mergers at early times and for the less massive SRs that they have been Virgo members since the cluster formation. Therefore, since SRs are preferentially located towards the core and highest-density regions of the Virgo cluster, they would be more prone to undergo the high-velocity flybys than FRs and hence have more extended haloes.

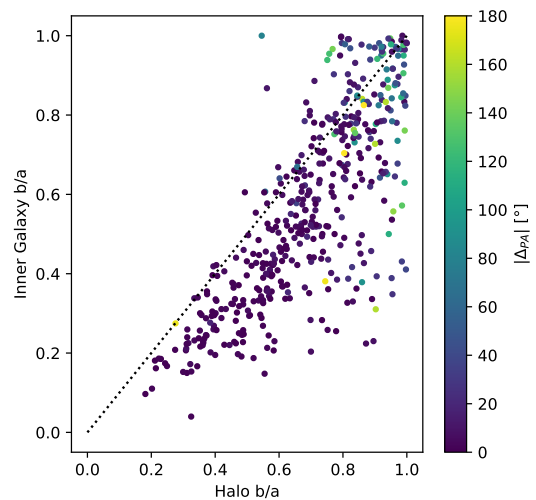


Figure 15. Apparent shapes of the annotated haloes. The axis ratio b/a of the galaxy is plotted against the axis ratio of its halo. Points are colour-coded by the difference of position angle (in degrees) between the ellipse representing the main galaxy and the ellipse of the halo.

9.2 Impact of internal ghost reflections

Our images suffer from various sources of pollution. In particular, the scattered light from luminous objects like foreground stars or the bright centre of galaxies can cause multiple internal reflections on the CCD and generate large artificial haloes around the source in the image, referred to as ghost reflections (Slater et al. 2009). Although ghost reflections from bright stars (i.e., ‘external ghosts’) can easily be delineated and removed from our analysis, the additional amount of ghost light from the bright galactic centre (‘internal ghosts’) is more difficult to tackle (e.g., Karabal et al. 2017), as it is mixed with the intrinsic light from the stellar halo. We evaluate the impact of these internal ghosts on our stellar haloes annotations. We remind that for our results presented in Sections 4, 5, 6, 7 and 8 we kept all haloes including the potentially problematic ones, and we did not correct for the effects studied below.

9.2.1 Shapes of haloes

Stellar haloes affected by internal ghost reflections from the galactic centre may first be identified by their specific shapes. Round haloes with a diameter similar to that of external ghost reflections from bright stars (with a typical radius of 3.5 arcmin for MATLAS, Karabal et al. 2017) are more susceptible to be contamination.

We can check this using the *Jafar* annotations of haloes, particularly comparing their axis ratio b/a to that of the inner galaxies. In Figure 15, we plot these axis ratios colour-coded by the difference in position angle between the halo and the inner galaxy. A high difference in position angle or a halo that is much rounder than the inner galaxy can pinpoint a problematic case. Several galaxies in our sample fall into this category.

9.2.2 PSF deconvolution

To properly quantify the effect of the reflections, we have deconvolved the images. This time consuming task, done only for a sub-sample of galaxies, was first required to model the Point Spread Function (PSF), in particular its critical outer wings. We used the PSF database com-

piled by Karabal et al. (2017) for MegaCam images. As deconvolution removes the additional light from internal ghosts, PSF-corrected haloes are expected to be smaller and less luminous. These effects are essential for haloes whose size is close to the size of the PSF, as the PSF wings are mixed with the outskirts of galaxies.

We have annotated the haloes of 36 galaxies in MATLAS images that were PSF-corrected with the method of Karabal et al. (2017) and compared the annotations with those obtained with the initial images. Figure 16 presents the difference in area and flux for the haloes of the original and deconvolved images. Haloes of the deconvolved images are, on a median, 24% smaller than the original ones. This value is high and most likely gives an upper limit of the PSF effect. Although we use a regularisation process to minimise the noise level in the deconvolved images, there is always an additional noise in the resulting images. This additional noise makes the identification of the outer isophotes more complicated and may lead to the annotation of slightly smaller haloes. Larger offsets for haloes with a size close to that of the PSF (around 3.5 arcmin) were expected and indeed observed as an increased scatter at that specific radius (see the left panel of Figure 16).

As shown in the right panel of Figure 16, PSF-corrected haloes have median values 15% less luminous, with a higher scatter around three arcmin. Since the median halo luminosity accounts for 10.6% of the total galaxy luminosity (see Section 4.2), the impact of the PSF on the total galaxy light is less than 2%. Our result is consistent with the 1.6% that Karabal et al. (2017) found for the external parts of their simulated galaxy. Trujillo & Fliri (2016) also find similar results for their haloes, with the original halo accounting for 11% of the total galaxy light, but only 3% for the PSF-corrected halo.

Another way of representing the impact of the PSF is to study the shapes of the haloes before and after deconvolution as a function of the original halo size. This is illustrated in Figure 17.

Two galaxies exhibit noticeable differences in halo size. NGC4026 (original radius of 3.5') is a typical example of a halo wrongly annotated due to PSF effects; the original halo is round and similar to a ghost halo, while the PSF-corrected one is much more elliptical. NGC2594 (original radius of 1.5') overlaps with a bright star, so the deconvolution removed a part of the halo that overlaps with the star.

10 SUMMARY AND CONCLUSIONS

Low surface brightness stellar structures around galaxies hold crucial clues about their late assembly history of the host galaxies. In this paper, we investigated the relationships between several quantitative properties of LSB structures (tidal features, extended stellar haloes) and the host galaxy properties (mass, environment, and internal kinematics) for a sample of 475 nearby massive galaxies.

Using the annotation tool Jafar (Sola et al. 2022), we have manually delineated LSB features around our 475 galaxies in deep images from four CFHT surveys: MATLAS, CFIS, VESTIGE and NGVS. Our galaxy sample, drawn from the ATLAS^{3D} reference catalogue (Cappellari et al. 2011a), contains similar numbers of ETGs and LTGs and probes the field, group and Virgo cluster. From our compiled database of 11832 annotated structures, including 199 tails and 100 streams, we quantitatively characterised LSB features' properties and coordinates in Table B2 and in Appendix B. The results we report are obtained for a surface brightness limit of about 29 mag arcsec⁻². Our catalogue of LSB features and their properties can be used as a baseline for future studies aiming to characterise tidal features and compare them to numerical simulation predictions. Our annotated structure dataset also provides labelled data for train-

ing machine learning algorithms to automatically find tidal features in deep images (Richards et al. 2022).

We summarise our results below.

a) Incidence and luminosity of LSB features

- 36% of our galaxies display one or more tidal features: 23% host tidal tails, 15% host streams and 12% host shells (Section 4.1).
- Tidal tails and streams account for 2-4% of the total galaxy luminosity and haloes for about 13% for ETGs and 8% for LTGs (Section 4.1). A PSF deconvolution is required for more accurate photometric measurements. For example, we calculate that the PSF makes our halos 15% more luminous (Section 9.2).
- Streams are fainter than tails, with a median surface brightness of 26.8 and 26.1 mag arcsec⁻², respectively. The faintest tidal feature is about one magnitude brighter than the SB limit.

The impact of mass, environment and internal kinematics on the incidence and luminosity of the tidal features and haloes were studied separately, though they might be linked. This issue is discussed in Section 7.

b) Trends with galaxy mass

- The fraction of galaxies hosting debris increases with galaxy mass, doubling from around 25% to 60% for the highest-mass galaxies. This trend is visible for each type of debris (Figure 3).
- More massive galaxies host more luminous tidal features (Section 5.1).
- More massive ETGs host haloes twice as luminous as less massive ones, while no evolution is seen for LTGs (Figure 5).
- There is a mass threshold around $4 - 7 \times 10^{10} M_{\odot}$ above which the slopes of the trends mentioned above are steeper (Figures 3 and 5).

c) Trends with the environment

- The large-scale environment (field/group versus Virgo cluster) does not impact the fraction of galaxies hosting tidal features (Figure 6).
- The presence of a nearby companion (in projected separation) leads to increased fractions of galaxies with tidal tails in the field/group and in the Virgo cluster (Figure 6).
- The large-scale environment does not affect the haloes of ETGs. However, LTGs have brighter haloes in the Virgo cluster (Figure 7), which could be interpreted as a sign of ram-pressure stripping and on-going outside-in star formation quenching (Section 6.2).

d) Trends with internal kinematics

- The fraction of slow rotators (42%) hosting debris is higher than that of fast rotators (33%).
- Slow rotators have haloes almost twice as luminous ($f_{L,halo} = 23\%$) than that of fast rotators ($f_{L,halo} = 12\%$).

These trends could, however, be due to the mass effect previously identified, as slow rotators are more massive than fast rotators. A proper analysis is needed to study the correlations at fixed mass and environment density.

To summarise, our quantitative analyses of LSB features around hundreds of massive galaxies enabled us to obtain hints about their recent assembly history. Our findings are consistent with the hierarchical build-up of galaxies, with massive galaxies having assembled the majority of their mass through mergers rather than by gas accretion. Mass, rather than the environment, is the dominant factor

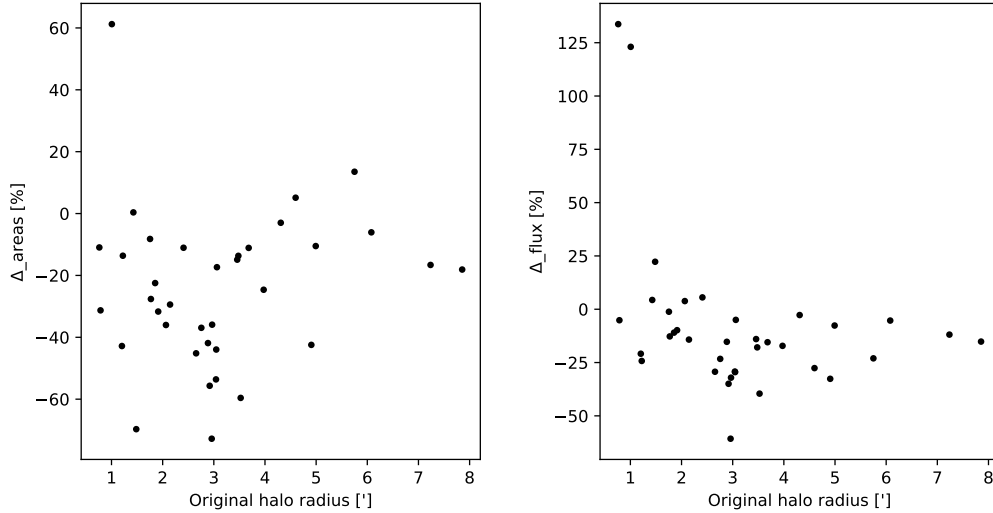


Figure 16. Impact of PSF deconvolution on the area and fluxes of the annotated haloes. *Left:* Percentage of difference between the area of the PSF-corrected and original haloes as a function of the radius of the original halo (in arcminutes). *Right:* Percentage of difference between the flux of PSF-corrected and original haloes, as a function of the radius of the original halo in arcminutes.

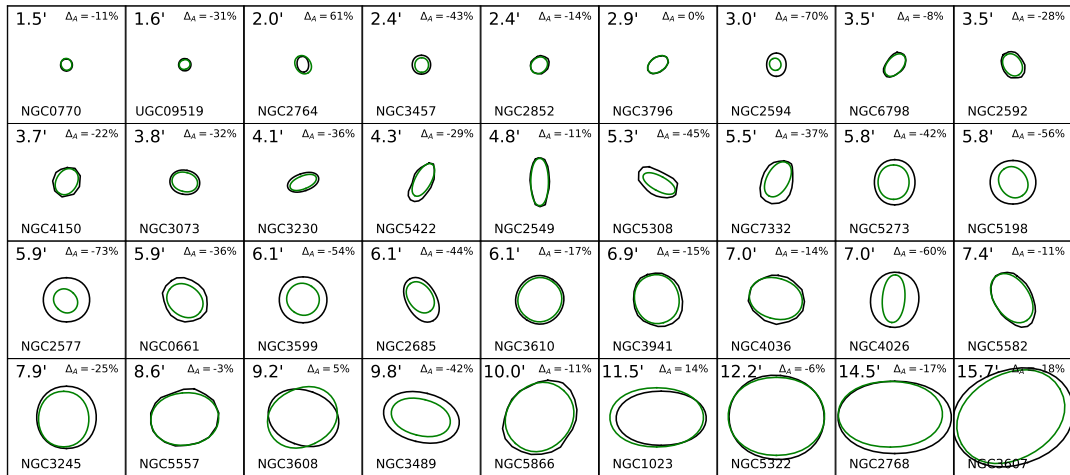


Figure 17. Comparison of the contours of the original (in black) and PSF-corrected (in green) haloes. Each box has a fixed size of 15 arcmin, and haloes are ordered by increasing original radius. The name of the galaxy is indicated at the bottom of each box and its original diameter (in arcminute) is indicated on the top left. The percentage of difference between the haloes areas before and after deconvolution is indicated as Δ_A in the top right.

that affects tidal features and haloes. More massive galaxies have undergone more mergers and thus show more signs of tidal disruption and brighter haloes (continuously formed from the phase-mixing of old tidal features). This is especially true for ETGs, which depend on galaxy mass. The presence of a mass threshold, also noted in the literature, is consistent with a picture where galaxy growth is dominated by gas accretion for low-mass galaxies and by mergers for high-mass galaxies, where gas accretion may no longer be possible.

Finally, the comparison of observations to the predictions of numerical simulations is one of the future important challenges, and our findings can be used for that purpose. Such work will require larger samples of LSB features, for which efficient automated methods still have to be developed.

DATA AVAILABILITY

To ensure the reproducibility of this work, we share in Appendix B the properties of the individual 199 tidal tails and 100 streams used in this study. We complement this by providing a file in the DS9 Region format that contains the coordinates of the contours of all our LSB features, including tails, streams, shells, haloes and inner galaxies. These can be used to create the mask of each annotation.

ACKNOWLEDGEMENTS

E.S. would like to thank Eric Emsellem for interesting discussions and for his thorough review of the paper which helped improve it. We thank Ariane Lançon for her comments on this work. We thank Maarten Baes, Crescenzo Tortora and Ivana Ebrova for providing mock images from the Illustris TNG50 and TNG100 simulations.

E.S is grateful to the Leverhulme Trust for funding under the grant number RPG-2021-205. M.P. is supported by the Academy of Finland grant n:o 347089. O.M. is grateful to the Swiss National Science Foundation for financial support under the grant number PZ00P2_202104. M.B. is grateful for the visiting professorship from the University of Vienna. R.H. acknowledges funding from the Italian INAF Large Grant 12-2022.

This research has made use of the SIMBAD database, operated at CDS, Strasbourg, France, and of "Aladin sky atlas" developed at CDS, Strasbourg Observatory, France. This work is based on data obtained as part of the Canada-France Imaging Survey, a CFHT large program of the National Research Council of Canada and the French Centre National de la Recherche Scientifique. Based on observations obtained with MegaPrime/MegaCam, a joint project of CFHT and CEA Saclay, at the Canada-France-Hawaii Telescope (CFHT) which is operated by the National Research Council (NRC) of Canada, the Institut National des Sciences de l'Univers (INSU) of the Centre National de la Recherche Scientifique (CNRS) of France, and the University of Hawaii. This research used the facilities of the Canadian Astronomy Data Centre operated by the National Research Council of Canada with the support of the Canadian Space Agency. This research is based in part on data collected at Subaru Telescope, which is operated by the National Astronomical Observatory of Japan. We are honored and grateful for the opportunity of observing the Universe from Maunakea, which has the cultural, historical and natural significance in Hawaii. Pan-STARRS is a project of the Institute for Astronomy of the University of Hawaii, and is supported by the NASA SSO Near Earth Observation Program under grants 80NSSC18K0971, NNX14AM74G, NNX12AR65G, NNX13AQ47G, NNX08AR22G, YORPD20_2-0014 and by the State of Hawaii. This research was supported by the International Space Science Institute (ISSI) in Bern, through ISSI International Team project #534.

REFERENCES

- Abraham R. G., van Dokkum P. G., 2014, *PASP*, **126**, 55
- Abraham R. G., van den Bergh S., Nair P., 2003, *ApJ*, **588**, 218
- Adams S. M., Zaritsky D., Sand D. J., Graham M. L., Bildfell C., Hoekstra H., Pritchett C., 2012, *AJ*, **144**, 128
- Agertz O., Teyssier R., Moore B., 2009, *MNRAS*, **397**, L64
- Alabi A. B., Romanowsky A. J., Forbes D. A., Brodie J. P., Okabe N., 2020, *MNRAS*, **496**, 3182
- Amorisco N. C., 2016, *Monthly Notices of the Royal Astronomical Society*, **464**, 2882
- Arp H., 1966, *ApJS*, **14**, 1
- Atkinson A. M., Abraham R. G., Ferguson A. M. N., 2013, *ApJ*, **765**, 28
- Balcells M., Quinn P. J., 1990, *ApJ*, **361**, 381
- Barnes J. E., 1988, *ApJ*, **331**, 699
- Bauch C. M., Benson A. J., Cole S., Frenk C. S., Lacey C., 2003, in Bender R., Renzini A., eds, *The Mass of Galaxies at Low and High Redshift*. p. 91 ([arXiv:astro-ph/0203051](https://arxiv.org/abs/astro-ph/0203051)), doi:10.1007/10899892_22
- Bekki K., 1999, *ApJ*, **510**, L15
- Bekki K., 2009, *MNRAS*, **399**, 2221
- Belokurov V., et al., 2006, *ApJ*, **642**, L137
- Berrier J. C., Stewart K. R., Bullock J. S., Purcell C. W., Barton E. J., Wechsler R. H., 2008, *The Astrophysical Journal*, **690**, 1292
- Bertin E., Arnouts S., 1996, *A&AS*, **117**, 393
- Bickley R. W., et al., 2021, *MNRAS*, **504**, 372
- Bilek M., et al., 2020, *MNRAS*, **498**, 2138
- Bilek M., Duc P. A., Sola E., 2023, *A&A*, **672**, A27
- Binggeli B., Tammann G. A., Sandage A., 1987, *AJ*, **94**, 251
- Bois M., et al., 2011, *Monthly Notices of the Royal Astronomical Society*, **416**, 1654
- Borlaff A., et al., 2019, *A&A*, **621**, A133
- Boselli A., Gavazzi G., 2006, *PASP*, **118**, 517
- Boselli A., Boissier S., Cortese L., Gil de Paz A., Seibert M., Madore B. F., Buat V., Martin D. C., 2006, *ApJ*, **651**, 811
- Boselli A., et al., 2014, *A&A*, **570**, A69
- Boselli A., et al., 2018, *A&A*, **614**, A56
- Boselli A., Fossati M., Sun M., 2022, *A&ARv*, **30**, 3
- Bridge C. R., Carlberg R. G., Sullivan M., 2010, *ApJ*, **709**, 1067
- Bullock J. S., Johnston K. V., 2005, *ApJ*, **635**, 931
- Byrd G., Valtonen M., 1990, *ApJ*, **350**, 89
- Cantiello M., et al., 2018, *ApJ*, **856**, 126
- Cappellari M., 2008, *MNRAS*, **390**, 71
- Cappellari M., et al., 2011a, *MNRAS*, **413**, 813
- Cappellari M., et al., 2011b, *MNRAS*, **416**, 1680
- Cappellari M., et al., 2013a, *MNRAS*, **432**, 1709
- Cappellari M., et al., 2013b, *MNRAS*, **432**, 1862
- Casteels K. R. V., et al., 2013, *MNRAS*, **429**, 1051
- Cayatte V., van Gorkom J. H., Balkowski C., Kotanyi C., 1990, *AJ*, **100**, 604
- Chambers K. C., et al., 2016, arXiv e-prints, p. [arXiv:1612.05560](https://arxiv.org/abs/1612.05560)
- Chung A., van Gorkom J. H., Kenney J. D. P., Crowl H., Vollmer B., 2009, *AJ*, **138**, 1741
- Cole S., Lacey C. G., Baugh C. M., Frenk C. S., 2000, *MNRAS*, **319**, 168
- Conroy C., Wechsler R. H., Kravtsov A. V., 2007, *ApJ*, **668**, 826
- Conselice C. J., 2009, *MNRAS*, **399**, L16
- Conselice C. J., Bershady M. A., Dickinson M., Papovich C., 2003, *AJ*, **126**, 1183
- Cooper A. P., et al., 2010, *MNRAS*, **406**, 744
- Cooper A. P., D'Souza R., Kauffmann G., Wang J., Boylan-Kolchin M., Guo Q., Frenk C. S., White S. D. M., 2013, *MNRAS*, **434**, 3348
- Daddi E., et al., 2007, *ApJ*, **670**, 156
- Dekel A., Birnboim Y., 2006, *MNRAS*, **368**, 2
- Dekel A., Sari R., Ceverino D., 2009, *ApJ*, **703**, 785
- Di Matteo P., Pipino A., Lehnert M. D., Combes F., Semelin B., 2009, *A&A*, **499**, 427
- Dressler A., 1980, *ApJ*, **236**, 351
- Duc P.-A., 2020, arXiv e-prints, p. [arXiv:2007.13874](https://arxiv.org/abs/2007.13874)
- Duc P.-A., Renaud F., 2013, in Souchay J., Mathis S., Tokieda T., eds, , Vol. 861, *Lecture Notes in Physics*, Berlin Springer Verlag. p. 327, doi:10.1007/978-3-642-32961-6_9
- Duc P.-A., et al., 2011, *MNRAS*, **417**, 863
- Duc P.-A., et al., 2015, *MNRAS*, **446**, 120
- Durret F., Chiche S., Lobo C., Jauzac M., 2021, *A&A*, **648**, A63
- Ebrova I., 2013, arXiv e-prints, p. [arXiv:1312.1643](https://arxiv.org/abs/1312.1643)
- Ebrova Ivana e. a., in prep
- Elias L. M., Sales L. V., Creasey P., Cooper M. C., Bullock J. S., Rich R. M., Hernquist L., 2018, *MNRAS*, **479**, 4004
- Emsellem E., et al., 2007, *MNRAS*, **379**, 401
- Emsellem E., et al., 2011, *MNRAS*, **414**, 888
- Euclid Collaboration et al., 2022, *A&A*, **657**, A92
- Fernique P., Boch T., Donaldson T., Durand D., O'Mullane W., Reinecke M., Taylor M., 2014, MOC - HEALPix Multi-Order Coverage map Version 1.0, IVOA Recommendation 02 June 2014 ([arXiv:1505.02937](https://arxiv.org/abs/1505.02937)), doi:10.5479/ADS/bib/2014ivoa.spec.0602F
- Fernique P., et al., 2015, *A&A*, **578**, A114
- Ferrarese L., et al., 2012, *ApJS*, **200**, 4
- Förster Schreiber N. M., et al., 2009, *ApJ*, **706**, 1364
- Fossati M., et al., 2013, *A&A*, **553**, A91
- Gavazzi G., Boselli A., Scodreggio M., Pierini D., Belsole E., 1999, *MNRAS*, **304**, 595
- Genel S., Bouché N., Naab T., Sternberg A., Genzel R., 2010, *The Astrophysical Journal*, **719**, 229
- Gilhuly C., et al., 2022, *ApJ*, **932**, 44
- Gnedin O. Y., 2003, *ApJ*, **582**, 141
- Goto T., Yamauchi C., Fujita Y., Okamura S., Sekiguchi M., Smail I., Bernardi M., Gomez P. L., 2003, *MNRAS*, **346**, 601
- Gunn J. E., Gott J. Richard I., 1972, *ApJ*, **176**, 1
- Hendel D., Johnston K. V., 2015, *MNRAS*, **454**, 2472
- Henriksen M., Byrd G., 1996, *ApJ*, **459**, 82
- Hernquist L., Quinn P. J., 1987, *ApJ*, **312**, 1

- Hester J. A., 2006, *The Astrophysical Journal*, 647, 910
- Hill A. R., et al., 2017a, *ApJ*, 837, 147
- Hill A. R., Muzzin A., Franx M., Marchesini D., 2017b, *ApJ*, 849, L26
- Hilz M., Naab T., Ostriker J. P., 2013, *MNRAS*, 429, 2924
- Hodges J. L., 1958, *Arkiv for Matematik*, 3, 469
- Hood C. E., Kannappan S. J., Stark D. V., Dell'Antonio I. P., Moffett A. J., Eckert K. D., Norris M. A., Hendel D., 2018, *The Astrophysical Journal*, 857, 144
- Huang Q., Fan L., 2022, *ApJS*, 262, 39
- Ibata R., Irwin M., Lewis G., Ferguson A. M. N., Tanvir N., 2001a, *Nature*, 412, 49
- Ibata R., Lewis G. F., Irwin M., Totten E., Quinn T., 2001b, *ApJ*, 551, 294
- Ibata R. A., et al., 2017, *ApJ*, 848, 128
- Iodice E., et al., 2021, *The Messenger*, 183, 25
- Jackson T. M., Pasquali A., La Barbera F., More S., Grebel E. K., 2021, arXiv e-prints, p. arXiv:2102.02241
- Janowiecki S., Mihos J. C., Harding P., Feldmeier J. J., Rudick C., Morrison H., 2010, *ApJ*, 715, 972
- Ji I., Peirani S., Yi S. K., 2014, *A&A*, 566, A97
- Johnston K. V., Majewski S. R., Siegel M. H., Reid I. N., Kunkel W. E., 1999, *AJ*, 118, 1719
- Johnston K. V., Bullock J. S., Sharma S., Font A., Robertson B. E., Leitner S. N., 2008, *ApJ*, 689, 936
- Kado-Fong E., et al., 2018, *ApJ*, 866, 103
- Karabal E., Duc P. A., Kuntschner H., Chanial P., Cuillandre J. C., Gwyn S., 2017, *A&A*, 601, A86
- Karademir G. S., Remus R.-S., Burkert A., Dolag K., Hoffmann T. L., Moster B. P., Steinwandel U. P., Zhang J., 2019, *MNRAS*, 487, 318
- Kauffmann G., White S. D. M., Guiderdoni B., 1993, *MNRAS*, 264, 201
- Kauffmann G., et al., 2003, *MNRAS*, 341, 54
- Kaviraj S., 2010, *MNRAS*, 406, 382
- Kawata D., Mulchaey J. S., 2008, *ApJ*, 672, L103
- Kereš D., Katz N., Weinberg D. H., Davé R., 2005, *MNRAS*, 363, 2
- Khalid A., Brough S., Martin G., Kimmig L. C., Lagos C. D. P., Remus R. S., Martínez-Lombilla C., 2024, *MNRAS*, 530, 4422
- Khochfar S., et al., 2011, *MNRAS*, 417, 845
- Kim T., et al., 2012, *ApJ*, 753, 43
- Kluge M., et al., 2020, *ApJS*, 247, 43
- Koopmann R. A., Kenney J. D. P., 2004, *ApJ*, 613, 866
- Krajnović D., et al., 2011, *MNRAS*, 414, 2923
- L'Huillier B., Combes F., Semelin B., 2012, *A&A*, 544, A68
- Lagos C. d. P., Schaye J., Bahé Y., van de Sande J., Kay S. T., Barnes D., Davis T. A., Dalla Vecchia C., 2018, *MNRAS*, 476, 4327
- Lagos C. d. P., Emsellem E., van de Sande J., Harborne K. E., Cortese L., Davison T., Foster C., Wright R. J., 2022, *MNRAS*, 509, 4372
- Larson R. B., Tinsley B. M., Caldwell C. N., 1980, *ApJ*, 237, 692
- Lim S., Cote P., Peng E., Ferrarese L., Ngvs Team Matlas Team 2023, in American Astronomical Society Meeting Abstracts. p. 258.03
- Lotz J. M., Primack J., Madau P., 2004, *AJ*, 128, 163
- Lux H., Read J. I., Lake G., Johnston K. V., 2013, *MNRAS*, 436, 2386
- Magnier E. A., Cuillandre J. C., 2004, *PASP*, 116, 449
- Malin D. F., Carter D., 1983, *ApJ*, 274, 534
- Mancillas B., Duc P.-A., Combes F., Bournaud F., Emsellem E., Martig M., Michel-Dansac L., 2019, *A&A*, 632, A122
- Mantha K. B., et al., 2019, *MNRAS*, 486, 2643
- Marinacci F., et al., 2017, arXiv e-prints, p. arXiv:1707.03396
- Martin N. F., et al., 2014, *ApJ*, 787, 19
- Martin G., Kaviraj S., Hocking A., Read S. C., Geach J. E., 2020, *MNRAS*, 491, 1408
- Martin G., et al., 2022, *MNRAS*, 513, 1459
- Martínez-Delgado D., et al., 2010, *AJ*, 140, 962
- Martínez-Delgado D., et al., 2021, arXiv e-prints, p. arXiv:2104.06071
- Mastropietro C., Moore B., Mayer L., Debattista V. P., Piffaretti R., Stadel J., 2005, *MNRAS*, 364, 607
- McCarthy I. G., Font A. S., Crain R. A., Deason A. J., Schaye J., Theuns T., 2012, *MNRAS*, 420, 2245
- McConnachie A. W., et al., 2009, *Nature*, 461, 66
- Mei S., et al., 2007, *ApJ*, 655, 144
- Merritt A., van Dokkum P., Abraham R., Zhang J., 2016, *ApJ*, 830, 62
- Mihos J. C., 1995, *ApJ*, 438, L75
- Mihos J. C., 2003, arXiv e-prints, pp astro-ph/0305512
- Mihos J. C., 2004, The Evolution of Tidal Debris (arXiv:astro-ph/0401557), doi:10.48550/arXiv.astro-ph/0401557
- Mihos J. C., Harding P., Feldmeier J., Morrison H., 2005, *ApJ*, 631, L41
- Miskolczi A., Bomans D. J., Dettmar R. J., 2011, *A&A*, 536, A66
- Montes M., 2019, arXiv e-prints, p. arXiv:1912.01616
- Mood A., 1950, Introduction to the Theory of Statistics, McGraw-Hill, pp 394–399
- Moore B., Katz N., Lake G., Dressler A., Oemler A., 1996, *Nature*, 379, 613
- Moore B., Lake G., Katz N., 1998, *ApJ*, 495, 139
- Morales G., Martínez-Delgado D., Grebel E. K., Cooper A. P., Javanmardi B., Miskolczi A., 2018, *A&A*, 614, A143
- Mosenkov A., et al., 2020, *MNRAS*, 494, 1751
- Müller O., et al., 2019, *A&A*, 624, L6
- Naab T., Johansson P. H., Ostriker J. P., 2009, *ApJ*, 699, L178
- Naab T., et al., 2014, *MNRAS*, 444, 3357
- Naiman J. P., et al., 2017, arXiv e-prints, p. arXiv:1707.03401
- Nair P. B., Abraham R. G., 2010, *ApJS*, 186, 427
- Nelson D., et al., 2017, arXiv e-prints, p. arXiv:1707.03395
- Nelson D., et al., 2019, arXiv e-prints, p. arXiv:1902.05554
- Nevin R., Blecha L., Comerford J., Simon J., Terrazas B. A., Barrows R. S., Vázquez-Mata J. A., 2023, arXiv e-prints, p. arXiv:2303.06249
- Newman A. B., Ellis R. S., Bundy K., Treu T., 2012, *ApJ*, 746, 162
- Ocvirk P., Pichon C., Teyssier R., 2008, *Monthly Notices of the Royal Astronomical Society*, 390, 1326
- Oemler Augustus J., 1974, *ApJ*, 194, 1
- Oser L., Ostriker J. P., Naab T., Johansson P. H., Burkert A., 2010, *ApJ*, 725, 2312
- Pawlik M. M., Wild V., Walcher C. J., Johansson P. H., Villforth C., Rowlands K., Mendez-Abreu J., Hewlett T., 2016, *MNRAS*, 456, 3032
- Pearson K., 1895, *Proceedings of the Royal Society of London*, 58, 240–242
- Pearson W. J., Wang L., Trayford J. W., Petrillo C. E., van der Tak F. F. S., 2019, *A&A*, 626, A49
- Penoyre Z., Moster B. P., Sijacki D., Genel S., 2017, *MNRAS*, 468, 3883
- Pillepich A., et al., 2014, *MNRAS*, 444, 237
- Pillepich A., et al., 2017, arXiv e-prints, p. arXiv:1707.03406
- Pillepich A., et al., 2019, arXiv e-prints, p. arXiv:1902.05553
- Poggianti B. M., et al., 2016, *AJ*, 151, 78
- Pop A.-R., Pillepich A., Amorisco N. C., Hernquist L., 2018, *MNRAS*, 480, 1715
- Priest J. L., 1990, Status of shell galaxies.. pp 72–83
- Prunet S., Fouque S., Gwyn S., 2015, Photometric calibration of Megacam data, <https://www.cfht.hawaii.edu/Instruments/Imaging/MegaPrime/PDFs/megacam.pdf>
- Purcell C. W., Bullock J. S., Zentner A. R., 2007, *ApJ*, 666, 20
- Quinn P. J., 1984, *ApJ*, 279, 596
- Rich R. M., et al., 2019, *MNRAS*, 490, 1539
- Richards F., Sola E., Paiement A., Xie X., Duc P.-A., 2022, IEEE International Conference on Image Processing (ICIP)
- Richards F., Paiement A., Xie X., Sola E., Duc P.-A., 2023, 18th International Conference on Machine Vision Applications, Jul 2023, Hamamatsu, Shizuoka, Japan, hal-04129549
- Robotham A. S. G., et al., 2014, *MNRAS*, 444, 3986
- Rodríguez-Gomez V., et al., 2015, *MNRAS*, 449, 49
- Rodríguez-Gomez V., et al., 2016, *MNRAS*, 458, 2371
- Román J., Trujillo I., Montes M., 2020, *A&A*, 644, A42
- Rudick C. S., Mihos J. C., McBride C., 2006, *ApJ*, 648, 936
- Rudick C. S., Mihos J. C., Frey L. H., McBride C. K., 2009, *ApJ*, 699, 1518
- Rutherford T. H., et al., 2024, *MNRAS*,
- Sancisi R., Fraternali F., Oosterloo T., van der Hulst T., 2008, *A&ARv*, 15, 189
- Sanderson R. E., et al., 2018, *ApJ*, 869, 12
- Schulze F., Remus R.-S., Dolag K., 2017, *Galaxies*, 5
- Schweizer F., Seitzer P., 1988, *ApJ*, 328, 88
- Sheen Y.-K., Yi S. K., Ree C. H., Lee J., 2012, *ApJS*, 202, 8
- Sinha M., Holley-Bockelmann K., 2012, *ApJ*, 751, 17

- Slater C. T., Harding P., Mihos J. C., 2009, *PASP*, **121**, 1267
- Sola Elisabeth e. a., in prep
- Sola E., et al., 2022, *A&A*, **662**, A124
- Spearman C., 1904, *American Journal of Psychology*, **15**, 72–101
- Spitler L. R., et al., 2019, arXiv e-prints, p. [arXiv:1911.11579](https://arxiv.org/abs/1911.11579)
- Springel V., Hernquist L., 2005, *ApJ*, **622**, L9
- Springel V., et al., 2017, arXiv e-prints, p. [arXiv:1707.03397](https://arxiv.org/abs/1707.03397)
- Stewart K. R., Bullock J. S., Wechsler R. H., Maller A. H., Zentner A. R., 2008, *ApJ*, **683**, 597
- Stringer M. J., Benson A. J., 2007, *MNRAS*, **382**, 641
- Student 1908, *Biometrika*, p. 1–25
- Tal T., van Dokkum P. G., Nelan J., Bezanson R., 2009, *AJ*, **138**, 1417
- Thomas D., Greggio L., Bender R., 1999, *MNRAS*, **302**, 537
- Thomas G. F., Famaey B., Ibata R., Lüghausen F., Kroupa P., 2017, *A&A*, **603**, A65
- Toomre A., 1977, in Tinsley B. M., Larson Richard B. Gehret D. C., eds, *Evolution of Galaxies and Stellar Populations*. p. 401
- Toomre A., Toomre J., 1972, *ApJ*, **178**, 623
- Trujillo I., Fliri J., 2016, *ApJ*, **823**, 123
- Vázquez-Mata J. A., et al., 2022, *MNRAS*, **512**, 2222
- Venhola A., et al., 2017, *A&A*, **608**, A142
- Vulcani B., et al., 2016, *ApJ*, **816**, 86
- Walmsley M., Ferguson A. M. N., Mann R. G., Lintott C. J., 2019, *MNRAS*, **483**, 2968
- Wen Z. Z., Zheng X. Z., 2016, *ApJ*, **832**, 90
- White S. D. M., Frenk C. S., 1991, *ApJ*, **379**, 52
- Wright A. C., et al., 2023, arXiv e-prints, p. [arXiv:2309.10039](https://arxiv.org/abs/2309.10039)
- Yoon Y., Lim G., 2020, *ApJ*, **905**, 154
- Yoon Y., Ko J., Kim J.-W., 2023, *ApJ*, **946**, 41
- Yoon Y., Ko J., Chung H., Byun W., Chun K., 2024, Shell-type Tidal Features Are More Frequently Detected in Slowly Rotating Early-type Galaxies than Stream- and Tail-type Features ([arXiv:2404.03459](https://arxiv.org/abs/2404.03459))
- van Dokkum P. G., 2005, *AJ*, **130**, 2647

Table A1. Sample of galaxies studied in this work. The full table is available electronically from the CDS databases. Column (1): Galaxy name. Column (2): Right ascension (degree). Column (3): Declination (degree). Column (4): Morphological type. Column (5): Distance (in Mpc). Column (6): Stellar mass (in M_{\odot}), computed as described in Section 5. Column (7): Projected half-light effective radius in arcsecond. Column (8): Environmental density ρ_{10} (in Mpc^{-3}), i.e. mean density of galaxies inside a sphere centred on the galaxy and containing the 10 nearest neighbors. Column (9): Virgo cluster membership (1 if the galaxy is in Virgo, 0 otherwise). Column (10): Survey from which the image was taken. Column (11): Photometric bands available. Column (12): Small-scale environment of the galaxy, defined in Section 6: 1 if the galaxy is isolated, 0 if it is in pair (i.e. there is an annotated nearby companion susceptible to produce tidal interactions). Values in columns (1),(2),(3),(4),(5),(7) and (9) are drawn from Cappellari et al. (2011a), while Column (8) is from Cappellari et al. (2011b). When a galaxy was imaged by several surveys in different bands, they are all listed. However, all the annotations were made on the reference r -band image, and on the deepest available image (i.e., MATLAS rather than CFIS when both surveys were available).

Galaxy	RA	Dec	Type	D	Mass	$\log_{10}(R_e)$	$\log_{10}(\rho_{10})$	Virgo	Survey	Bands	Isolated
(1)	[deg]	[deg]	(4)	[Mpc]	[M_{\odot}]	[$''$]	[Mpc^{-3}]	(9)	(10)	(11)	(12)
IC0560	146.472	-0.269	ETG	27.2	9.81e+09	1.11	-1.91	0	MATLAS	rg	1
IC0598	153.202	43.146	ETG	35.3	1.61e+10	1.02	-2.31	0	MATLAS	rg	1
IC0676	168.166	9.056	ETG	24.6	1.41e+10	1.35	-1.41	0	MATLAS	rg	1
IC0719	175.077	9.01	ETG	29.4	3.75e+10	1.1	-1.91	0	MATLAS	r	0
IC0750	179.718	42.722	LTG	36.8	1.24e+11	1.24	-2.29	0	CFIS	r	0
⋮	⋮	⋮	⋮	⋮	⋮	⋮	⋮	⋮	⋮	⋮	⋮
UGC09519	221.588	34.371	ETG	27.6	1.01e+10	0.87	-2.45	0	MATLAS	rg	1
UGC09665	225.385	48.32	LTG	40.3	2.08e+10	1.11	-1.71	0	CFIS	r	0
UGC09703	226.359	46.565	LTG	39.1	9.27e+09	1.07	-1.59	0	CFIS	r	1
UGC09741	227.14	52.296	LTG	39.6	7.43e+09	1.16	-1.98	0	CFIS	r	1
UGC09858	231.673	40.564	LTG	40.9	2.93e+10	1.24	-2.33	0	CFIS	r	1

APPENDIX A: GALAXY SAMPLE

This section describes our sample of 475 galaxies. Table A1 provides a description of some properties of the galaxies. Figures A1 and A2 display color-composite thumbnails generated from true-colour PanSTARRS images and greyscale deep CFHT images, for ETGs and LTGs, respectively.

The stellar mass is computed differently for ETGs and LTGs. Following Cappellari et al. (2013a), ETGs are characterised by their dynamical mass M_{JAM} estimated by Jeans anisotropic modelling (JAM) (Cappellari 2008). The relation between the stellar mass of ETGs $M_{\star,\text{ETG}}$, the total galaxy luminosity L , the mass-to-light ratio $(M/L)_{\text{JAM}}$ and dynamical mass M_{JAM} is given by $M_{\text{JAM}} \equiv L \times (M/L)_{\text{JAM}}$ and $M_{\star,\text{ETG}} \approx 0.87 M_{\text{JAM}}$. The 0.87 factor linking stellar and dynamical masses comes from the estimated median fraction of dark matter mass of 13% enclosed in M_{JAM} (Cappellari et al. 2013a). M_{JAM} has the advantage of being more precise than stellar mass estimated from luminosity, as it does not require assumptions on the initial mass function, even though an assumption on the fraction of dark matter is needed. For LTGs, we did not have such M_{JAM} values, so we estimated their stellar mass $M_{\star,\text{LTG}}$ from their K -band luminosity L_K and the stellar mass-to-light ratio $(M/L)_K$, as $M_{\star,\text{LTG}} = (M/L)_K \times L_K$, assuming a fixed $(M/L)_K = 0.8 M_{\odot}/L_{\odot}$ from Cappellari et al. (2013b). The assumed $(M/L)_K$ ensures agreement between M_{JAM} and the K -band luminosity at the lowest masses (Cappellari et al. 2013b).

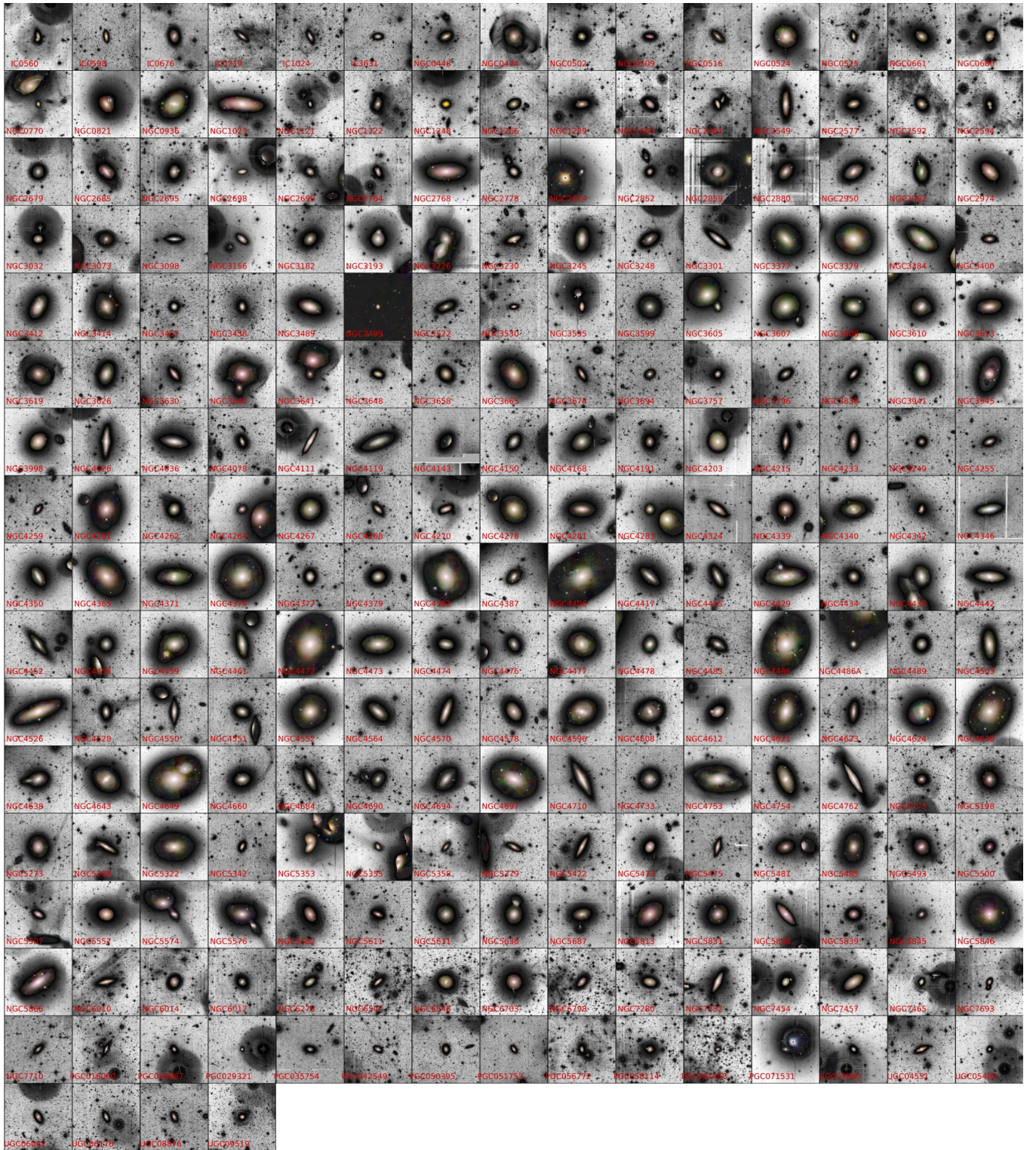


Figure A1. Color-composite image of the ETGs in our final sample. The forefront true-color image is taken from PanSTARRS r, g, i images and displays the galaxies as seen in shallow surveys. The greyscale image shows the extent of the galaxy as seen in deep CFHT observations. The field of view is 0.1 degree.

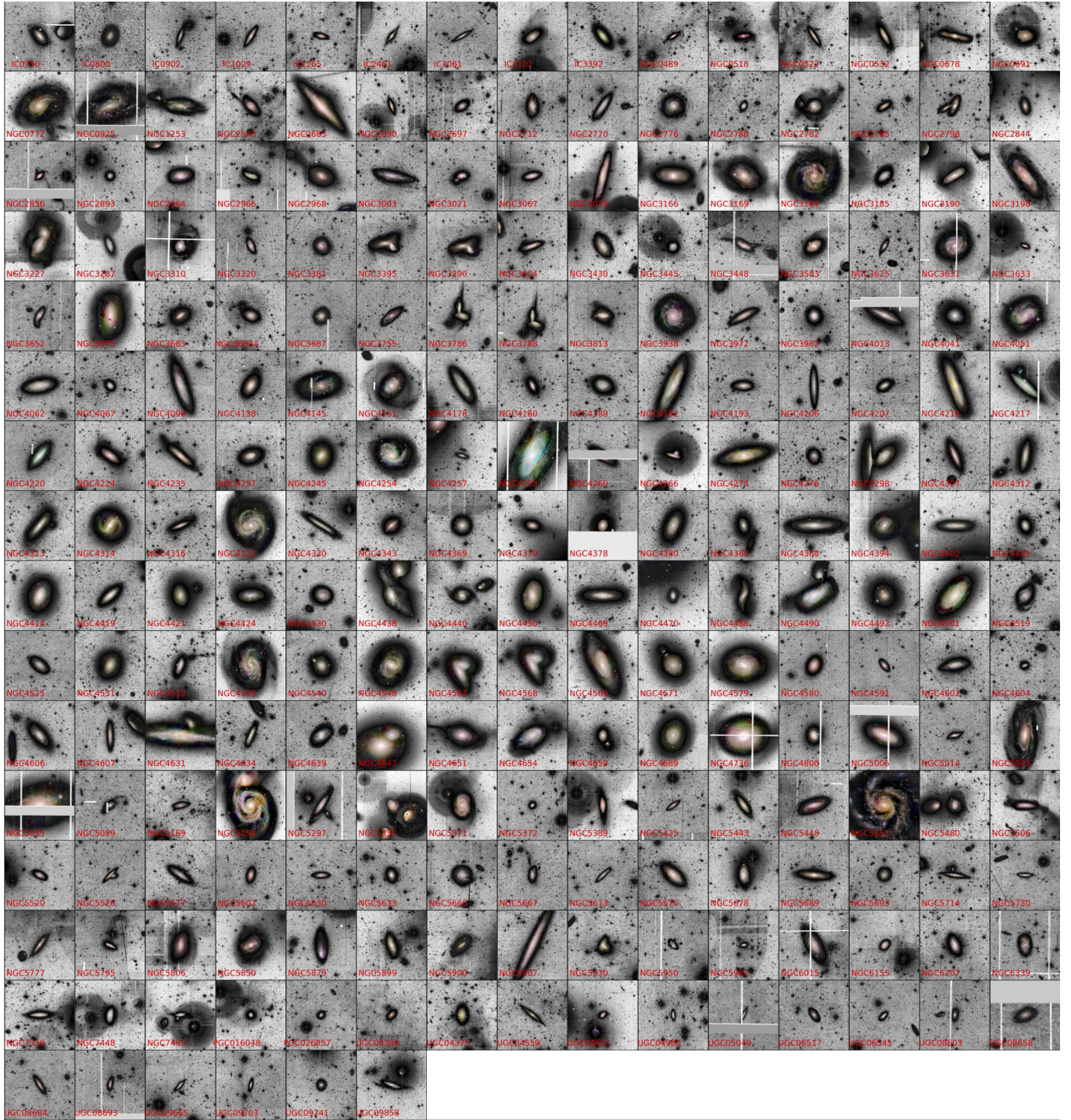


Figure A2. Color-composite image of the LTGs in our final sample, alphabetically ordered. The forefront RGB image is taken from PanSTARRS r , g , i images and displays the galaxies as seen in shallow surveys. The greyscale image shows the extent of the galaxy as seen in deep CFHT observations. The field of view is 0.1 degree.

Table B1. Number of tidal features per galaxy and halo properties. The computation of the number of tidal features per galaxy is explained in Section 4.1. The full table is available electronically at CDS databases. Column (1): Galaxy name. Column (2): Number of tidal tails. Column (3): Number of streams. Column (4): Number of shells. Column (5): Halo length (kpc). Column (6): Halo area (kpc²). Column (7): Halo area normalised with respect to the area of the *Inner Galaxy*. Column (8): Median surface brightness along the external contour of the halo (mag arcsec⁻²). Column (9): Percentage of the total galaxy flux contained in the halo.

Galaxy	# tails	# streams	# shells	Halo length	Halo area	Halo area	Halo SB	Halo flux
(1)	(2)	(3)	(4)	[kpc]	[kpc ²]	[Normalised]	[mag arcsec ⁻²]	[%]
IC0560	0	0	0.0	20.5	169.1	5.8	26.3	9.7
IC0598	0	0	0.0	24.3	231.6	4.8	27.3	0.5
IC0676	0	0	0.0	26.6	429.3	4.3	27.2	10.8
IC0719	0	0	0.0	23.5	161.9	3.5	26.7	3.0
IC0750	0	0	0.0	47.7	1018.7	5.0	26.4	4.4
⋮	⋮	⋮	⋮	⋮	⋮	⋮	⋮	⋮
UGC09519	0	0	4.0	27.1	553.3	36.8	27.4	7.1
UGC09665	0	0	0.0	27.5	214.4	2.9	26.6	3.1
UGC09703	0	0	0.0	24.4	174.4	4.2	26.6	9.3
UGC09741	0	0	0.0	23.1	394.6	7.5	27.0	17.1
UGC09858	2	0	0.0	68.5	1153.6	3.5	26.5	13.0

Table B2. The list of the individual annotated tidal tails and streams. The full table is available electronically at CDS databases. Column (1): identification number of the feature. Column (2): Feature type. Column (3): Galaxy name. Column (4): Length (kpc). Column (5): Area (kpc²). Column (6): Area normalised with respect to the area of the *Inner Galaxy*. Column (7): Median surface brightness (mag arcsec⁻²) inside the annotation. Column (8): Percentage of the total galaxy flux contained in that feature.

Feature #	Type	Galaxy	Length	Area	Area	SB	Flux
(1)	(2)	(3)	[kpc]	[kpc ²]	[Normalised]	[mag arcsec ⁻²]	[%]
1	Stream	IC1024	49.4	270.8	9.9	27.3	2.6
2	Stream	IC1024	32.4	126.5	4.6	27.5	1.0
3	Stream	IC3102	25.9	113.0	1.6	26.2	2.7
4	Stream	NGC0474	135.1	751.6	3.7	25.3	21.6
5	Stream	NGC0474	59.7	176.0	0.9	26.0	0.9
⋮	⋮	⋮	⋮	⋮	⋮	⋮	⋮
295	Stream	UGC05408	17.1	43.0	1.5	27.4	0.2
296	Tail	UGC08693	11.3	39.7	0.6	26.5	0.7
297	Tail	UGC08693	15.9	34.4	0.5	25.4	2.2
298	Tail	UGC09858	32.2	160.8	0.5	25.1	2.5
299	Tail	UGC09858	26.4	104.0	0.3	25.3	3.7

APPENDIX B: INDIVIDUAL FEATURES

In Table B1, we provide the number of tidal features identified per galaxy, along with the area, length, surface brightness and flux of the halo. In Table B2, we provide the list of the individual 199 tidal tails and 100 streams that were kept after our selection process.

To ensure full reproducibility of our results, and as a complement to Table B2, we provide a file in the DS9 Region format that contains the coordinates of our LSB features: tails, streams, shells, haloes and inner galaxies. An truncated example is shown below, while the full version is available electronically in the CDS databases. The file lists the identification number of the feature, the host galaxy, the type of feature and the coordinates of its contours, which are given in the format *polygon(ra₁,dec₁,ra₂,dec₂,...,ra_n,dec_n)*. This region file can be opened with SAOImageDS9 and Aladin. Arbitrary colours were associated to each feature type, e.g., red for *Stream*, blue for *Tidal Tails*, orange for *Shells*, green for *Haloes* and magenta for *Inner Galaxy*.

```
# Region file format: DS9 version 4.1
global color=yellow dashlist=8 3 width=1 font="helvetica 10 normal roman" select=1
highlite=1 dash=0 fixed=0 edit=1 move=1 delete=1 include=1 source=1
icrs
# Feature0 IC1024 Streams
polygon(217.859,3.02384,...,217.872,3.02806) # color=red
# Feature1 IC1024 Streams
```

```
polygon(217.849,3.05411,...,217.853,3.05204) # color=red  
# Feature2 IC3102 Streams  
polygon(184.33315,6.7513204,...,184.32008,6.7470474) # color=red  
# Feature3 NGC0474 Streams  
polygon(20.0919,3.56068,...,20.0848,3.55207) # color=red  
# Feature4 NGC0474 Streams  
polygon(20.034,3.34547,...,20.0243,3.34832) # color=red
```

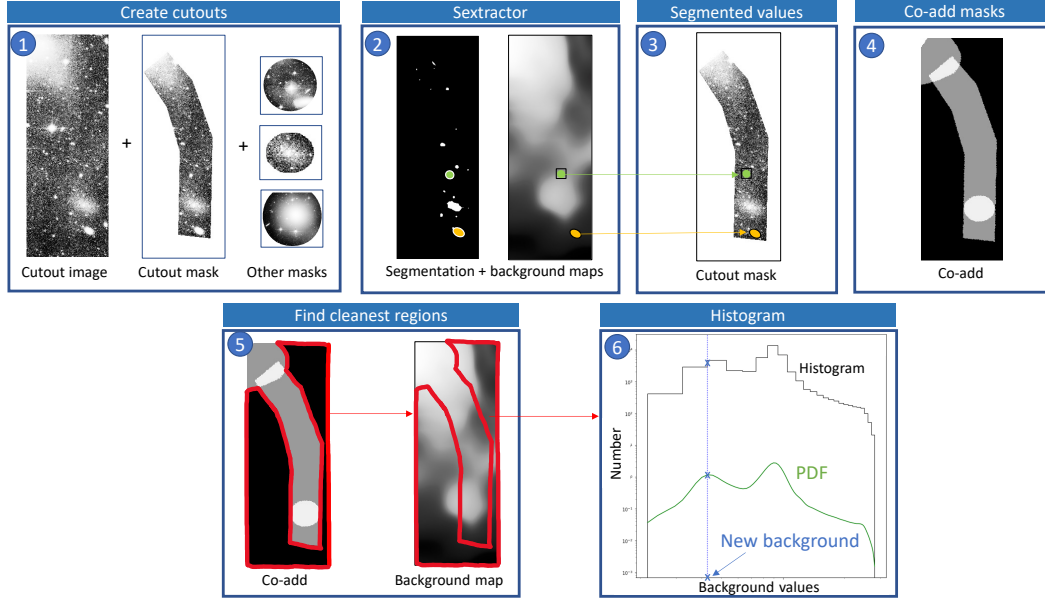



Figure C1. Illustration of the refined luminosity estimation process, for one stream feature around one galaxy. *Step 1:* the cutouts of the mask and image of the feature of interest are created, as well as masks of other annotations around the galaxy. *Step 2:* source extraction and background measurement are performed using SExtractor. Two segmented regions are highlighted in orange and green, to illustrate how the pixels will be replaced in the next step. *Step 3:* segmented pixels are replaced by the corresponding background map values. Two examples of such segmented regions are represented in green and orange. *Step 4:* the masks of the other annotations are co-added on the same field of view as the feature of interest. *Step 5:* the contours of the cleanest regions, with the least number of annotations overlapping, are retrieved from the co-add and applied to the background map. Here, the cleanest regions are represented inside the red contour. *Step 6:* inside the cleanest regions, the histogram of the background map values is created (in black). Then, the PDF is estimated (in green), and the peaks of the PDF are computed. Only the first significant peak is kept (in blue), and its value is taken as the new background value.

APPENDIX C: MASKS, BACKGROUND SUBTRACTION AND LUMINOSITY

In this section, we describe the method we used to obtain a better estimate of the luminosity and the SB of a structure. The process for one feature annotated by one contributor for a specific galaxy is divided in several steps, each of which are described below. An illustration of this process is presented in Figure C1.

The process starts with the creation of two cutouts (step 1): a mask showing only the feature (i.e. blank values outside the feature), and an image of the feature with its surroundings (i.e. a cropped version of the original image). Working with cutouts reduces the size of the files and the computation time required to process them. It must be noted that in the particular case of haloes, we only retained the region between the external border of the main galaxy and the external border of the halo, to remove the influence of the centre of the galaxy. Hence, our halo masks have ‘donut’ shapes when they are the feature of interest.

Then, mask cutouts of other annotations for the same contributor and the same galaxy are created: the entire halo²⁶, companion galaxies (including small dwarfs) and ghosted reflections. These annotations are important, as they might overlap with the feature of interest.

The next step is source extraction to remove bright foreground sources (step 2). The software SExtractor (Bertin & Arnouts 1996) was run in double mode on the feature of interest. The segmentation was done on the mask cutout, while the background measurement was done on the cutout image²⁷.

The pixels masked on the segmentation map are then replaced by the corresponding values from the background map, and then applied to the mask cutout (step 3). The last part of this step is a cleaning one. Indeed, there may be erroneous pixels in the mask cutout, due to artefacts from the instrument (like CCD gaps). After inspection on some initial test cases, these erroneous pixels have large negative values, so all the pixels with a value smaller than a given threshold are replaced by the corresponding pixels in the background map.

We re-estimate the background after the pixel replacement (steps 4 - 6). This step is important, as it enables a more precise background estimation, which is crucial when dealing with LSB features. The images are supposed to have a flat background equal to zero after being processed by Elixir-LSB. However, there may be local variations, due to contamination sources like bright stars or cirrus, that locally cause non-zero background values. We want to remove the influence of other structures, i.e. other annotations that may be overlapping with the feature of interest.

The re-estimation of the background starts with the co-addition of all the cutouts masks of the other annotations for that contributor and that galaxy, that were previously created during step 1. They are co-added and re-projected²⁸ to the same field of view as the feature of interest

²⁶ We use the term ‘entire halo’ to refer to the annotations that retain both the inner part of the main galaxy and the donut-shaped outer halo.

²⁷ After some tests, we used the following threshold for detection of tidal features: DETECT_THRESHOLD=2 and DETECT_THRESHOLD=12 for haloes. To estimate the background, we use the parameters BACK_PHOTOTYPE=Local and BACK_SIZE=32.

²⁸ The re-projection was done using the *reproject* Python package, <https://reproject.readthedocs.io/en/stable/>

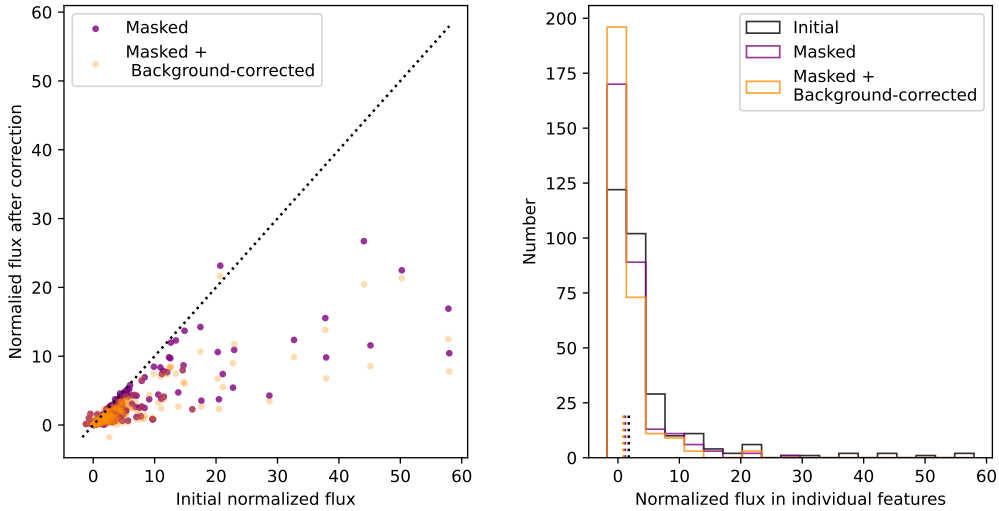


Figure C2. Comparison of the fraction of flux in individual tidal features (tails and streams), normalized with respect to the flux of the entire annotated halo. This fraction is computed on the initial cutout images, on the masked (i.e. bright sources masked) and on the final background-corrected (i.e. bright sources masked and background correction) images. *Left:* Scatter plot of the fraction of initial versus masked (in purple) and background-corrected (in orange) fluxes for each individual feature. *Right:* Histogram of the fraction of flux in tidal features, computed on the initial (in black), masked (in purple) and final background-corrected (in black) images.

(step 4). This co-add is applied on SExtractor’s background map. The cleanest regions, i.e. where there are no footprint of any annotation, are retrieved (step 5). In the case where there are annotations everywhere, the regions where there are the smallest number of overlapping annotations are kept. The new background is then evaluated in these cleanest regions. To that end, the histogram of the background map values in the cleanest regions is created (step 6), and the corresponding probability distribution function (PDF) is obtained from a kernel density estimation. As the PDF can be multimodal, it is not correct to simply keep the mean or mean value, nor the highest or smallest peak of the PDF. After some tests, we decided to use the first significant peak of the PDF as the new background value. A peak is considered significant if the computation of its prominence is higher than a given threshold.

Finally, the newly estimated background value is subtracted from all pixels in the cutout mask; at the end of this step the final cutout mask is obtained. From this final cutout mask, the flux f can be retrieved simply by summing all the pixels inside it. The luminosity L is obtained through the formula:

$$L = 4\pi \times D^2 \times f \quad (\text{C1})$$

where D is the distance of the galaxy and f the flux. Likewise, the SB can be computed from that final mask.

We now investigate the impact that masking of the bright sources and of our background correction can have on the retrieved flux of the features. To that end, we compare the flux in features in the initial (i.e., not masked, not background-corrected), masked (not background-corrected) and final (masked, background-corrected) cutout images. We normalise the flux in features (individual tails and streams) to the flux of the whole halo. Figure C2 presents the comparison.

It appears that the most crucial step of our method is masking the bright stars rather than the re-estimation of the background. Bright sources account for 67% of the flux of tidal features, while an additional 33% comes from not performing the background re-estimation. Indeed, the median (resp. mean) flux fraction in individual tidal features is 1.8% (resp. 4.5%) for the initial images; against 1.2% (resp. 2.4%) for the clean images and 0.9% (resp. 1.8%) for the background-corrected images.

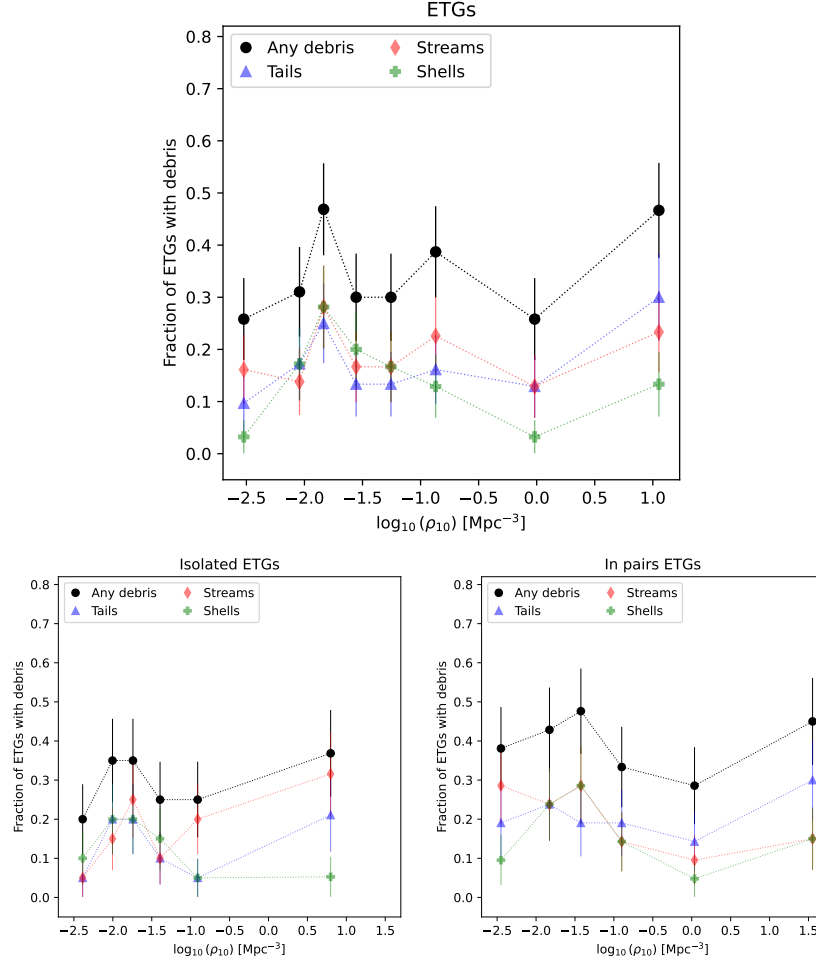


Figure D1. Fraction of ETGs that have tidal features as a function of the galaxy density ρ_{10} (in Mpc⁻³), per bin of ρ_{10} . Each bin contains approximately the same number of galaxies (i.e. about 30 galaxies per bin for the top plot, 20 for the bottom left and 21 for the bottom right). The fraction of ETGs hosting any type of debris is plotted in black, ETGs hosting tails in blue, streams in red and shells in green. The error bars represent the standard deviation on proportions in each bin. Galaxies in the Virgo cluster have $\log_{10}(\rho_{10}) > -0.4$. *Top:* Fraction of ETGs with debris considering all ETGs together. *Bottom left:* Fraction of ETGs with debris only considering isolated (i.e. post-merger) ETGs (see Section 6.1). *Bottom right:* Fraction of ETGs with debris only considering ETGs in pairs, i.e. that could be undergoing tidal interactions with a massive companion.

APPENDIX D: TRENDS AS A FUNCTION OF THE MORPHOLOGICAL TYPE

We complement the analyses of tidal features and stellar haloes by studying the trends as a function of the morphological type of the host galaxy, to determine whether this effect could be dominant. We investigate the fraction of galaxies hosting debris as a function of environmental density, separating post-merger galaxies from the ones in pairs, for ETGs and LTGs in Figures D1 and D2. These plots are complementary to Figure 6, with similar conclusions. We find hints of tidal feature generation in the group environment, with increased fractions of galaxies hosting all types of debris. Isolated galaxies do not show any prominent peak for the incidence of tidal features. Similar plots are shown in Figure D3 for the fraction of galaxies hosting debris as a function of galaxy mass. As in Figure 3, we see an increase of the fraction of galaxies hosting debris as a function of galaxy mass.

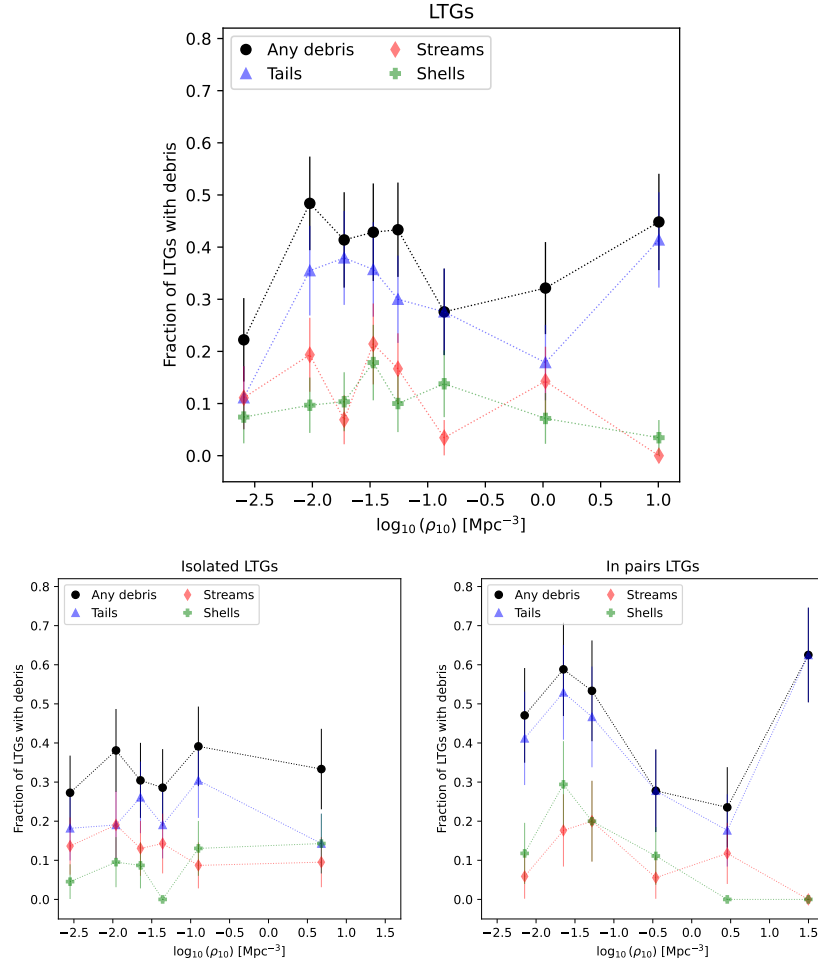


Figure D2. Fraction of LTGs that have tidal features as a function of the galaxy density ρ_{10} (in Mpc^{-3}), per bin of ρ_{10} . Each bin contains approximately the same number of galaxies (i.e. about 29 galaxies per bin for the top plot, 21 for the bottom left and 17 for the bottom right). The fraction of LTGs hosting any type of debris is plotted in black, LTGs hosting tails in blue, streams in red and shells in green. The error bars represent the standard deviation on proportions in each bin. Galaxies in the Virgo cluster have $\log_{10}(\rho_{10}) > -0.4$. *Top*: Fraction of LTGs with debris considering all LTGs together. *Bottom left*: Fraction of LTGs with debris only considering isolated (i.e. post-merger) LTGs (see Section 6.1). *Bottom right*: Fraction of LTGs with debris only considering LTGs in pairs, i.e. that could be undergoing tidal interactions with a massive companion.

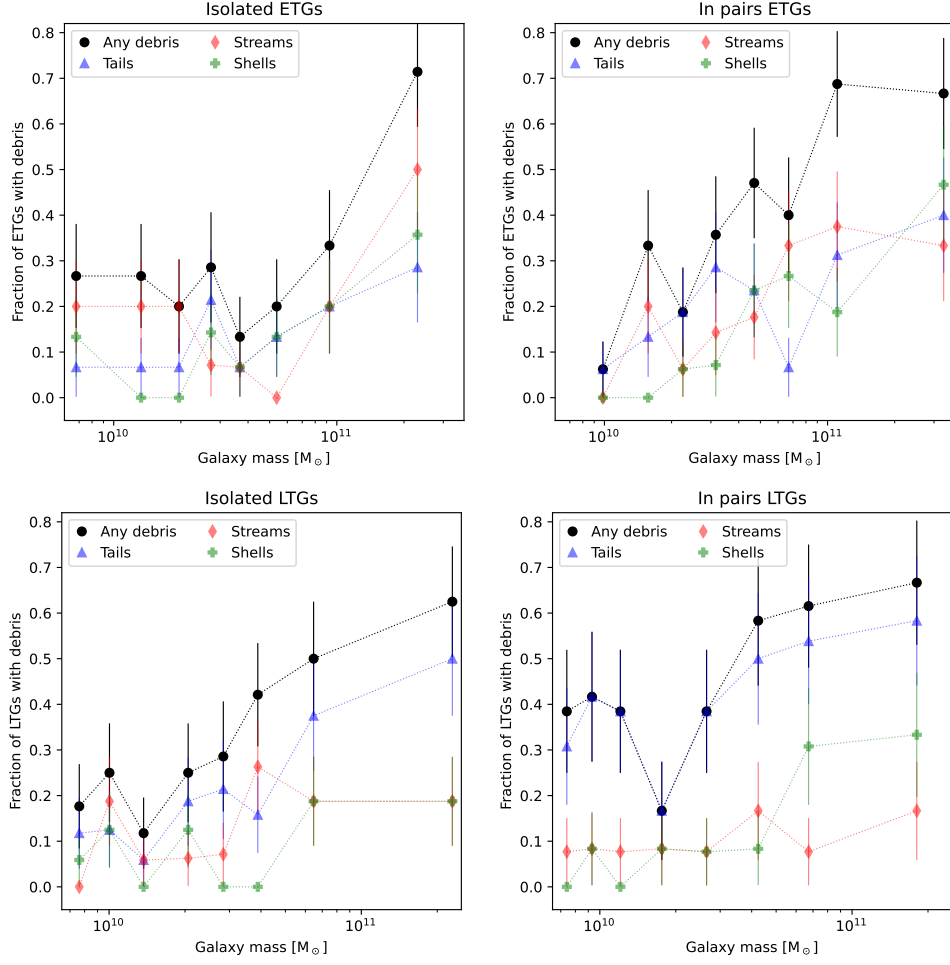


Figure D3. Fraction of ETGs (*top panel*) and LTGs (*bottom panel*) that have tidal features as a function of the galaxy stellar mass (in M_{\odot}), per mass bin. Each bin contains approximately the same number of galaxies (i.e. about 15 galaxies per bin for the top plots, 16 for the bottom left and 12 for the bottom right plot). The fraction of galaxies hosting any type of debris is plotted in black, galaxies hosting tails, in blue, streams in red and shells in green. The error bars represent the standard deviation on proportions in each bin. *Left column*: Fraction of galaxies with debris only considering isolated (i.e. post-merger) galaxies (see Section 6.1). *Right column*: Fraction of galaxies with debris only considering galaxies in pairs, i.e. that could be undergoing tidal interactions with a massive companion.

APPENDIX E: NOTE ON THE SURFACE BRIGHTNESS LIMIT

We indicated in Section 2 the surface brightness limits of MATLAS, CFIS and VESTIGE as reported in the literature. However these values were not computed in a consistent manner, which can lead to significance differences that are due to the method and not the image. Here, we recompute the surface brightness limits of the r -band images for these three surveys using the method described in Appendix A of Román et al. (2020).

As the value of the SB limit strongly depends on the image and the presence of contamination sources (e.g., cirrus, bright stars, ghost reflections), we visually select three ‘clean’ images per survey, at the original pixel scale. We mask all sources using SExtractor. We then randomly select fifty cutouts of varying size per masked image. For each cutout, we compute the histogram of the pixel values and fit a Gaussian to it. The resulting standard deviation σ is used to estimate $\mu_{lim,(3\sigma,10''\times 10'')}$, the surface brightness limit at the 3σ level on an angular scale of $10'' \times 10''$, as:

$$\mu_{lim,(3\sigma;10''\times 10'')} = -2.5 \times \log_{10} \left(\frac{3\sigma}{pix \times 10} \right) + zp \quad (E1)$$

where pix is the original pixel size and zp is the zeropoint.

We find that the re-computed $\mu_{lim,(3\sigma,10''\times 10'')}$ for MATLAS is around 29.2 mag arcsec⁻²; it is of 28.7 mag arcsec⁻² for CFIS and 29.1 mag arcsec⁻² for VESTIGE. For MATLAS, this value is slightly higher than the quoted 28.9 mag arcsec⁻² (Cuillandre, private communication), and the same is seen for CFIS (with a quoted 28.3 mag arcsec⁻², Cuillandre, private communication). A larger difference is seen for VESTIGE with a quoted 27.2 mag arcsec⁻² (Boselli et al. 2018). This clearly demonstrates that the choice of methodology can lead to very different results, and that the surface brightness limit is not relevant if not computed in the exact same way for all surveys. In addition, this limit depends on how clean the images are, so we could have obtained slightly different values had we chosen other images.

Nonetheless, the re-computed surface brightness limit enables us to compare our surveys. As expected, CFIS is shallower than MATLAS. VESTIGE reaches a depth similar to MATLAS, contrary to what was indicated with the SB limits in the literature, but this is not surprising after inspection of the images. Indeed, we noted that VESTIGE images looked very similar to NGVS (that has a depth similar to MATLAS) and even better due to the absence of the prominent ghost reflections that polluted the older filter set of MegaCam, as discussed in Section F1. We emphasize again that the important point for our study is not an ill-defined surface brightness limit value, but the fact that all images come from the same instrument and same reduction pipeline, which made them appear relatively similar. Furthermore, the SB limit is not at all synonym of detection limit of the LSB features (e.g., Martín et al. 2020; Román et al. 2020).



Figure F1. Comparison between images of the same galaxies from NGVS *g*-band images (*top row*) and VESTIGE *r*-band images (*bottom row*), with the same stretch and size. From left to right, NGC4178, NGC4216, and NGC4438.

APPENDIX F: IMPACT OF THE CHANGE OF THE SET OF FILTERS

The filter set of the MegaCam camera was changed after 2014. The old filters were in place for MATLAS and NGVS, whereas for CFIS and VESTIGE the new filters were used. This has an important impact on the images that we assessed in this work. Indeed, the properties of these new broad-band *ugriz* filters differ from the old ones, with improved transmission properties (spatial and spectral), field of view and different central wavelengths

(Prunet et al. 2015).

This change has an impact on the shape and prominence of the ghost reflections as they depend on the filter, as discussed in Section 9.2. In Figure F1 we illustrate the fact that ghost reflections are much more prominent for the old MegaCam filters (MATLAS and NGVS) than for the new ones (VESTIGE and CFIS).

To assess this difference in a more quantitative way, we compared the cleanness of images of the same galaxies between NGVS (*g*-band, old filter) and VESTIGE (*r*-band, new filter)²⁹. To that end, we used the weighted reliability index defined in Sola et al. (2022); this number is based on the percentage of intersection between the annotation of the halo of a galaxy and annotations of sources of pollution (such as cirrus, bright ghost reflections, satellite trails). The higher the index, the cleaner the image. In Figure F2, we compare the weighted reliability index for the same galaxies annotated by a single contributor to have consistent annotations. It clearly appears that NGVS images are much more impacted by contamination sources such as ghosted haloes and bright stars; 72% of images have an index lower than 2. On the contrary, 43% of VESTIGE images are clear of any contamination source, and 33% have an index lower than 2. The new *r*-band filter images are much cleaner than NGVS, although *g*-band images are less affected by PSF contamination (i.e. less bright ghost reflections) than the *r*-band. The identification of tidal features is therefore on average easier in VESTIGE images, even though VESTIGE is less deep than NGVS. This shows that instrumental effects including internal reflections due to filters (new versus old) have almost as much of an impact as the depth of the survey in the detection and identification of tidal features.

We assessed the impact of the change of filter on the colour estimation. We selected four common fields in the MATLAS/CFIS and NGVS/VESTIGE surveys that were observed with the old and new *r*-band filter³⁰. We ran SExtractor on each field to automatically compute the segmentation maps, and we applied the same segmentation between the old and the new filters. We then performed a cross-match of the sources in order to select only the same regions in each pair of fields. From this, we only kept the segmented regions that were the cleanest, i.e. with a high enough signal-to-noise ratio, and which followed a relatively tight relation for the magnitude between the old and new filters. We called these kept ‘best points’ and we present their flux in the old and new filters in the left panel of Figure F3. A clear offset between the new and the old magnitudes is observed. It is not due to the variation of extinction in the 4 different fields, as shown in the middle panel of Figure F3.

Fitting a linear regression in order to convert the magnitudes from the new filter to the old filter, we derived the following conversion formula:

$$mag_{r,new2old} = 1.019 \times mag_{r,old} - 0.147 \quad (F1)$$

where $mag_{r,new2old}$ is the extinction and colour-corrected magnitude in the *r*-band new filter converted to be in the old filter, and $mag_{r,old}$ is the magnitude in the old filter. The ‘extinction and colour-corrected magnitude’ corresponds to the magnitude of the object when corrected both for extinction and for the change of MegaCam filters which required colour-correction. The effect of this correction is shown in the right panel of Figure F3.

²⁹ We compare these two bands as VESTIGE only has the *r*-band available and NGVS has very few *r*-band images.

³⁰ Only a few NGVS *r*-band images were available.

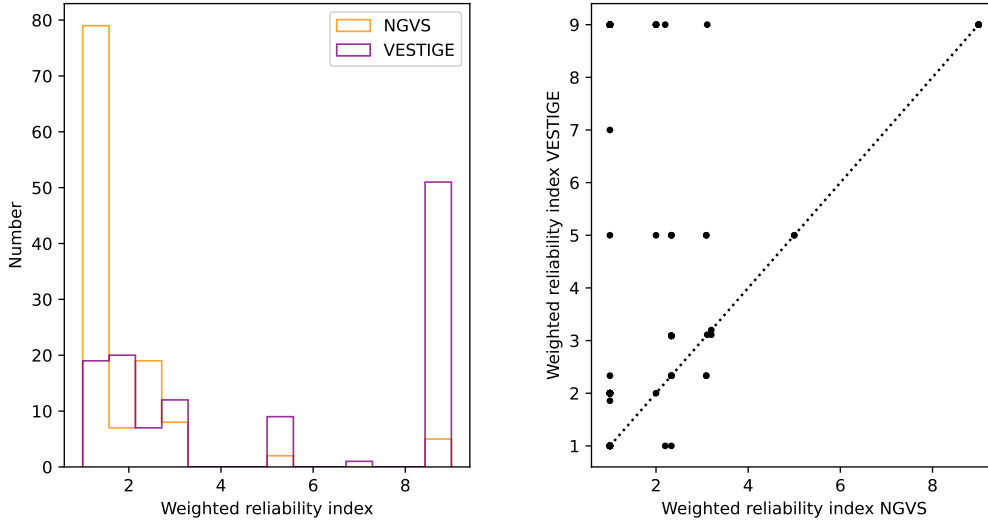


Figure F2. *Left:* Histogram of the weighted reliability index for NGVS (in orange) and VESTIGE (in purple). The higher the index, the cleaner the image. *Right:* Scatter plot of the weighted reliability index of VESTIGE as a function of the one for NGVS for the same fields.

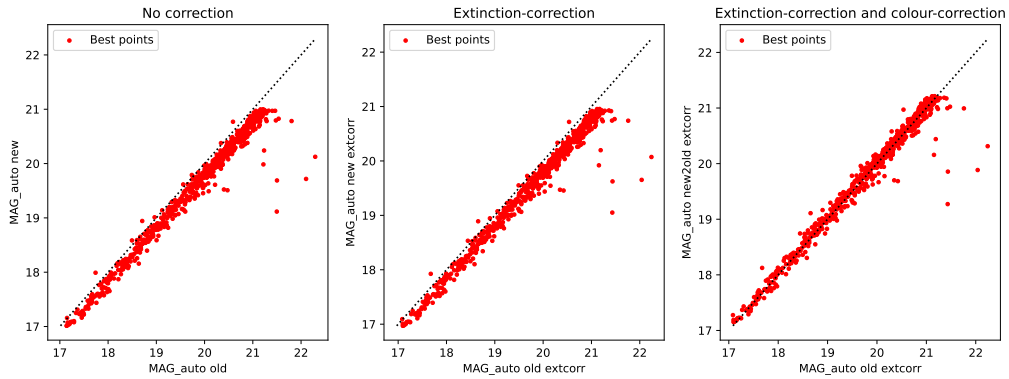


Figure F3. Estimation of the colour-correction between MegaCam old and new r -band filters, and effect of extinction correction. Magnitudes are expressed in mag. *Left:* Scatter plot of the magnitude in the new filter ($MAG_auto\ new$) as a function of the old filter ($MAG_auto\ old$) without extinction correction. *Middle:* Scatter plot of the magnitude in the new filter ($MAG_auto\ new\ extcorr$) as a function of the old filter ($MAG_auto\ old\ extcorr$) with extinction correction. *Right:* Scatter plot of the magnitude in the new filter for which the colour-correction has been applied ($MAG_auto\ new2old\ extcorr$) as a function of the old filter ($MAG_auto\ old\ extcorr$) with extinction correction and colour-correction.

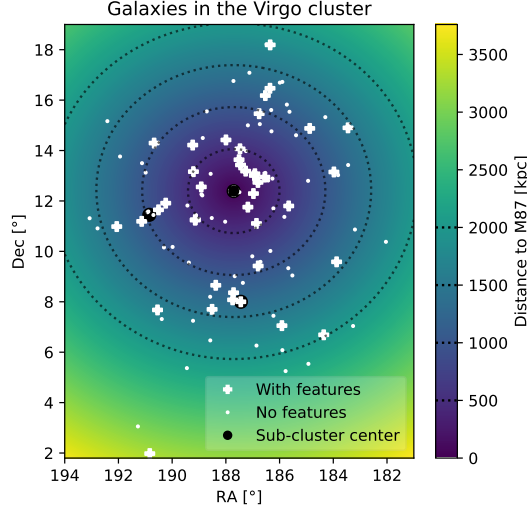


Figure G1. Spatial location of the galaxies (with and without tidal features) in the Virgo cluster, colour-coded by the distance to the cluster center, taken as M87. Black circles show the position of sub-clusters inside the Virgo cluster. The dotted lines correspond to distances of 500, 1000, 1500 and 2000 kpc.

APPENDIX G: IMPACT OF THE LOCATION INSIDE THE VIRGO CLUSTER

In this Section, we investigate the impact of the location of the galaxy inside the Virgo cluster on the fraction of galaxies hosting debris. In the left panel of Figure G1, we represent the location of the galaxies with and without tidal features, and their distance to the center of the Virgo cluster, taken as M87 (i.e. NGC4486). The dotted lines help visualising radii of 500, 1000, 1500 and 2000 kpc from M87. We compare the position of these galaxies to the location of the Virgo sub-clusters (black circles) from Figure 1 and Table 1 of Boselli et al. (2014). Galaxies hosting tidal features are more concentrated around the sub-cluster centers, i.e. in the densest regions.

In addition, in Figure G2 we present the fraction of Virgo galaxies hosting debris as a function of the distance to M87. We separate galaxies between isolated (middle plot, 38 out of 112 galaxies), in pairs (right plot, 74 out of 112 galaxies) and all galaxies together (left plot). When considering all galaxies together, there are two main trends. There is an increased fraction of galaxies with debris close to M87 (with a distance lower than 600 kpc). This trend is mostly driven by tidal tails, although streams contribute to that increase below 500 kpc and shells contribute from 500 - 600 kpc. Then, there is a decrease around 1000 kpc and another rise in the fraction of galaxies hosting debris between approximately 1100 - 1600 kpc from M87. When we compare this to the spatial location of the galaxies, these ‘peaks’ are correlated to the position of the sub-clusters. Furthermore, when we separate galaxies between isolated and in pairs (middle and left plot of Figure G2), we find again that these increases are actually due to on-going interactions. Isolated galaxies further away from the cluster center show less tidal features than the ones closer to M87. More precisely, the fraction of galaxies with tails or shells decreases with increasing distance, while the fraction of galaxies with streams increases with clustercentric distance. The global trend for isolated galaxies does not enable us to separate the effect of the processes generating features (e.g. tails near the center, streams at the outskirts) and the ones erasing them (e.g. streams near the center). Overall, the results suggest that the close proximity to other galaxies inside the Virgo cluster is responsible for the generation of tidal features. Yet, tidal feature evaporation is also hinted (with decreasing fraction of shells near the center) and could be due to repeated fast encounters (e.g., Moore et al. 1996, 1998), highlighting the competing processes at play in clusters.

These results are consistent with the strong dependence between some galaxy properties, like tidal features, and the position of the galaxies in the cluster, already noted in the literature (e.g., Gnedin 2003; Mihos 2004; Boselli & Gavazzi 2006; Janowiecki et al. 2010; Adams et al. 2012). For instance, Adams et al. (2012) reported a decrease in the fraction of galaxies with tidal feature closer to the clusters centers. They could not determine whether this was due to having more mergers near the clusters outskirts, or to shorter tidal feature lifetimes near the clusters centers. We do not see here such a decrease near the center; on the contrary we see increased fractions, especially of galaxies hosting tails due to close interactions. This discrepancy can be explained by the fact that we studied LTGs and ETGs, and tails are more prominent around LTGs. Then, we only have one cluster environment, Virgo being still dynamically young (e.g., Binggeli et al. 1987; Boselli et al. 2014), while Adams et al. (2012) targeted the ETGs of 54 clusters. In addition, our SB limit is deeper than their ($26.5 \text{ mag arcsec}^{-2}$ which makes us prone to detect more features. We also distinguish between the different categories of tidal disturbances which enables us to see different (sometimes opposite) trends depending on the feature type.

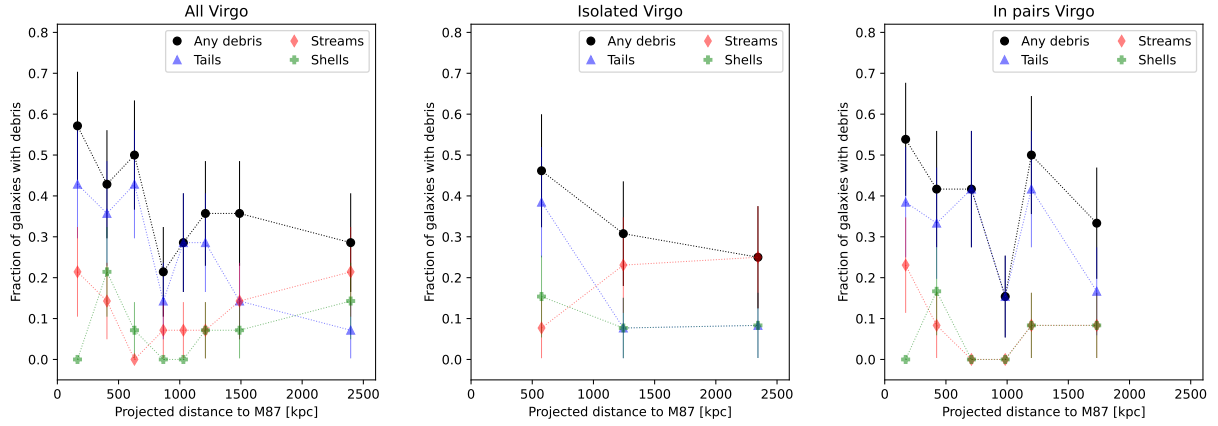


Figure G2. Fraction of galaxies in the Virgo cluster hosting tidal features as a function of the distance to the cluster center taken as M87 (in kpc), per distance bin. Each bin contains approximately the same number of galaxies (i.e. about 14 galaxies per bin for the right plot, 13 for the middle plot and 12 for the left plot). The fraction of galaxies hosting any type of debris is plotted in black, galaxies hosting tails, in blue, streams in red and shells in green. The error bars represent the standard deviation on proportions in each bin. *Left:* Fraction of galaxies with debris considering all galaxies in the Virgo cluster. *Middle:* Fraction of galaxies with debris only considering isolated galaxies (see Section 6.1). *Right:* Fraction of galaxies with debris only considering galaxies in pairs, i.e. that could be undergoing tidal interactions with a massive companion.

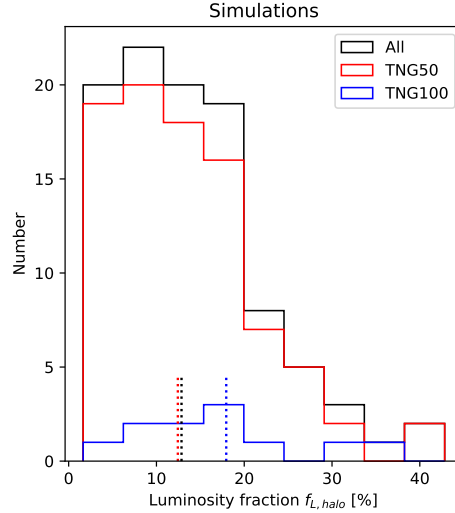


Figure H1. Histogram of the luminosity fraction in the haloes of galaxies in mock images from Illustris TNG50 (red), TNG100 (blue) and both simulations together (black). The vertical dotted line represent the median value of the distributions.

APPENDIX H: IMPACT OF THE HALO DEFINITION ON THE MEASUREMENTS: TESTS WITH MOCK SIMULATIONS

In this Paper, we estimate the luminosity fraction in haloes based on the contours of our annotations. Here, we investigate whether our method would give similar results when applied to mock images from numerical simulations. It must be noted that a proper analysis of simulated galaxies would require a large sample of hundreds of galaxies, using different cosmological simulations, as well as realistic mock images that include sources of contamination to be comparable to observations (e.g., Bickley et al. 2021).

For this test, we used mock images from the cosmological simulations Illustris TNG100 and Illustris TNG50. The Illustris TNG project (Nelson et al. 2017; Springel et al. 2017; Naiman et al. 2017; Marinacci et al. 2017; Pillepich et al. 2017, 2019; Nelson et al. 2019) is a suite of state-of-the-art cosmological galaxy formation simulations, which consist of three volumes simulations (i.e., cubic volumes of side length 50 Mpc (TNG50), 100 Mpc (TNG100), and 300 Mpc (TNG300)) that were run up to a redshift of zero. The TNG50 images were then adapted to match *Euclid* specifications in terms of photometric band (optical VIS) and resolution ($0.1''$ per pixel), a surface brightness limit of $29.5 \text{ mag arcsec}^{-2}$ has been applied, and galaxies were artificially placed at a distance of 82.5 Mpc. For TNG100, the images were produced in the i -band with a SB limit of $28.5 \text{ mag arcsec}^{-2}$, and galaxies were artificially placed at a distance of 40 Mpc. Additionally, we generated colour images (g, r, i) with a SB limit of $25 \text{ mag arcsec}^{-2}$ to simulate the shallow Pan-STARRS survey used in our study.

We selected a few galaxies (11 images from TNG100 and 89 images from TNG50) and we applied *Jafar* on these mock images to delineate the halo and inner galaxy as we did for observations. Using the masks of the annotations, we summed the flux inside the entire annotation, within the halo (i.e. the ‘donut’-shaped region between the halo outer boundary and the inner galaxy) and within the inner galaxy. The luminosity fraction of simulated haloes is shown in Figure H1.

The median (resp. mean) luminosity fraction for TNG50 haloes is 13.5% (resp. 12.4%), while for TNG100 haloes the values are slightly higher with a median (resp. mean) fraction of 17.5% (resp. 17.9%), though the sample size is more limited. We also note a halo-to-halo variability. When comparing these values to the right panel of Figure 2, we find that the median values of simulated haloes align with our observational findings where ETGs have a median fraction of 13.4% and LTGs of 8.2% and in both cases there is an important halo-to-halo variability.

Therefore, this test showed that our measurements of halo luminosity is comparable in observations and simulations, but in order to fully capture this effect we need large samples of simulated galaxies and realistic mock images, which is beyond the scope of this paper. The thorough analysis of a full suite of mock images from simulations will be carried out as part of the MATLAS collaboration (e.g., Mancillas et al. 2019; Ebrova prep; Sola prep) and within other large-scale collaborations.

This paper has been typeset from a $\text{\TeX}/\text{\LaTeX}$ file prepared by the author.